

 Open access • Posted Content • DOI:10.1101/2021.07.13.452161

## In situ imaging of bacterial membrane projections and associated protein complexes using electron cryo-tomography — [Source link](#)

Mohammed Kaplan, [Georges Chreifi](#), [Lauren Ann Metskas](#), [Janine Liedtke](#) ...+14 more authors

**Institutions:** [California Institute of Technology](#), [Leiden University](#), [University of Kentucky](#), [University of Southern California](#) ...+5 more institutions

**Published on:** 13 Jul 2021 - [bioRxiv](#) (Cold Spring Harbor Laboratory)

**Topics:** [Vesicle](#)

Related papers:

- [In situ imaging of bacterial outer membrane projections and associated protein complexes using electron cryo-tomography](#)
- [Clathrin-coated vesicles from brain have small payloads: A cryo-electron tomographic study](#)
- [Electron microscope tomography of native membranes.](#)
- [AFM visualization of cortical filaments/network under cell-bound membrane vesicles](#)
- [Interaction of Cryptococcus neoformans Extracellular Vesicles with the Cell Wall](#)

Share this paper:    

View more about this paper here: <https://typeset.io/papers/in-situ-imaging-of-bacterial-membrane-projections-and-141un27yo6>



26 **Abstract**

27 The ability to produce membrane projections in the form of tubular membrane extensions (MEs)  
28 and membrane vesicles (MVs) is a widespread phenomenon among bacteria. Despite this, our  
29 knowledge of the ultrastructure of these extensions and their associated protein complexes remains  
30 limited. Here, we surveyed the ultrastructure and formation of MEs and MVs, and their associated  
31 protein complexes, in tens of thousands of electron cryo-tomograms of ~ 90 bacterial species that  
32 we have collected for various projects over the past 15 years (Jensen lab database), in addition to  
33 data generated in the Briegel lab. We identified MEs and MVs in 13 species and classified several  
34 major ultrastructures: 1) tubes with a uniform diameter (with or without an internal scaffold), 2)  
35 tubes with irregular diameter, 3) tubes with a vesicular dilation at their tip, 4) pearling tubes, 5)  
36 connected chains of vesicles (with or without neck-like connectors), 6) budding vesicles and  
37 nanopods. We also identified several protein complexes associated with these MEs and MVs  
38 which were distributed either randomly or exclusively at the tip. These complexes include a  
39 secretin-like structure and a novel crown-shaped structure observed primarily in vesicles from  
40 lysed cells. In total, this work helps to characterize the diversity of bacterial membrane projections  
41 and lays the groundwork for future research in this field.

42

43

44

45

46

47

48

## 49 **Introduction**

50 Membrane extensions and vesicles (henceforth referred to as MEs and MVs) have been described  
51 in many types of bacteria. They are best characterized in diderms, where they stem mainly from  
52 the outer membrane (OM; we thus refer to OMEs and OMVs) and perform a variety of functions  
53 [1–4]. For example, the OMEs of *Shewanella oneidensis* (aka nanowires) are involved in  
54 extracellular electron transfer [5,6]. The OM tubes of *Myxococcus xanthus* are involved in the  
55 intra-species transfer of periplasmic and OM-associated material between different cells that is  
56 essential for the complex social behavior of this species [7–9]. The OMVs of *Vibrio cholerae* act  
57 as a defense mechanism, helping the bacterium circumvent phage infection [10]. A marine  
58 Flavobacterium affiliated with the genus *Formosa* (strain Hel3\_A1\_48) extrudes membrane tubes  
59 and vesicles that contain the type IX secretion system and digestive enzymes [11]. OMVs often  
60 function in pathogenesis. The OM blebs and vesicles of *Flavobacterium psychrophilum* have  
61 proteolytic activities that help release nutrients from the environment and impede the host immune  
62 system [12]. The OMVs of *Francisella novicida* contain virulence factors, suggesting they are  
63 involved in pathogenesis [13]. Similarly, the virulence of *Flavobacterium columnare* is associated  
64 with the secretion of OMVs [14], and membrane tubes and secreted vesicles have been observed  
65 in other, human pathogens like *Helicobacter pylori* and *Vibrio vulnificus* [15,16].

66  
67 MEs and MVs are also produced by monoderm bacteria and archaea. MVs stemming from the  
68 cytoplasmic membrane of Gram-positive bacteria have been reported to encapsulate DNA (see  
69 Ref. [17] and references therein.) Membrane nanotubes were recently discovered in the Gram-  
70 positive *Bacillus subtilis*, as well as the Gram-negative *Escherichia coli*. These nanotubes were  
71 found to connect two different bacterial cells and are involved in the transfer of cytoplasmic

72 material between bacterial cells of the same and different species, and even to eukaryotic cells  
73 [18–24].

74  
75 The structures of MEs and MVs are as varied as their functions. While *S. oneidensis* nanowires  
76 are chains of interconnected outer membrane vesicles with variable diameter and decorated with  
77 cytochromes [6], OM tubes of *H. pylori* have a fixed diameter of ~40 nm and are characterized by  
78 an inner scaffold and lateral ports [15]. *V. vulnificus* produces tubes from which vesicles ultimately  
79 pinch off by biopearling, forming a regular concentric pattern surrounding the cell [16]. Cells with  
80 an external surface layer (S-layer) can produce structures known as “nanopods,” which consist of  
81 membrane vesicles inside a sheath of S-layer. These have been reported in the soil-residing  
82 bacterium *Delftia* sp. Cs1-4 [25] and archaea of the order *Thermococcales* [26]. Finally, some  
83 diderms produce DNA-containing MVs consisting of both inner and outer membranes (see Ref.  
84 [4] and references therein).

85  
86 Different models have been proposed for how MEs and MVs form. In diderms, membrane  
87 blebbing may occur due to changes in the periplasmic turgor pressure, lipopolysaccharide  
88 repulsion or alterations in the contacts between the OM and the peptidoglycan cell wall [4]. Chains  
89 of interconnected vesicles are often observed, either as a result of direct vesicular budding from  
90 the OM or due to biopearling of membrane tubes [6,11]. Formation of tubes is thought to be a  
91 stabilizing factor as it results in smaller vesicles, with tubes pearling into distal chains of vesicles  
92 that eventually disconnect [27]. Other extensions may be formed by dedicated machinery.  
93 Interestingly, nanotubes involved in cytoplasmic exchange have been reported to be dependent on  
94 a conserved set of proteins involved in assembly of the flagellar motor known as the type III

95 secretion system core complex (CORE): FliP/O/Q/R and FlhA/B [18,24]. Recently, it was also  
96 shown that the formation of bacterial nanotubes significantly increases under stress conditions or  
97 in dying cells, caused by biophysical forces resulting from the action of the cell wall hydrolases  
98 LytE and LytF [28].

99

100 Structural studies of MEs and MVs have relied mainly on scanning electron microscopy (SEM),  
101 conventional transmission electron microscopy (TEM), and light (fluorescence) microscopy.  
102 While these methods have significantly advanced our understanding, they are limited in terms of  
103 the information they can provide. For instance, in SEM and conventional TEM, sample preparation  
104 such as fixation, dehydration, and staining disrupt membrane ultrastructure. While light  
105 microscopy can reveal important information about the dynamics and timescales on which MEs  
106 and MVs form (e.g. [29]), no ultrastructural details can be resolved; MEs and MVs of different  
107 morphology appear identical. Currently, only electron cryo-tomography (cryo-ET) allows  
108 visualization of structures in a near-native state inside intact (frozen-hydrated) cells with  
109 macromolecular (~5 nm) resolution. This method has already been invaluable in revealing the  
110 structures of several membrane extensions, including *S. oneidensis* nanowires [6], *H. pylori*  
111 nanotubes [15], *D. acidovorans* nanopods [25], *V. vulnificus* OMV chains [16], and more recently  
112 cell-cell bridges in the archaeon *Haloferax volcanii* [30].

113

114 To understand what membrane extensions exist in bacterial cells and how they might form, we  
115 undertook a survey of ~90 bacterial species, drawing on a database of tens of thousands of electron  
116 cryo-tomograms of intact cells collected by our group for various projects over the past 15 years  
117 [31,32], in addition to data generated in the Briegel lab. Our survey revealed membrane projections

118 in 13 bacterial species. These projections took various forms: 1) tubes with a uniform diameter  
119 and with an internal scaffold, 2) tubes with a uniform diameter and without a clear internal scaffold,  
120 3) tubes with a vesicular dilation at their tip (teardrop-like extensions), 4) tubes with irregular  
121 diameter or pearling tubes, 5) interconnected chains of vesicles with uniform neck-like connectors,  
122 6) budding or detached OMVs, and 7) nanopods. We also identified protein complexes associated  
123 with MEs and MVs in these species. These complexes were either randomly distributed on the  
124 MEs and MVs or exhibited a preferred localization at their tip.

125

126

127

128

129

130

131

132

133

134

135

136

137

138

139

140

141 **Results:**

142 We examined tens of thousands of electron cryo-tomograms of ~ 90 bacterial species collected in  
143 the Jensen lab for various projects over the past 15 years together with tomograms collected in the  
144 Briegel lab. Most cells were intact, but some had naturally lysed. Note that we make this  
145 classification based on the cells' appearance in tomograms; intact cells have an unbroken cell  
146 envelope, uniform periplasmic width, and consistently dense cytoplasm. In addition to cryo-  
147 tomograms of cells, this dataset also included naturally-shed vesicles purified from *S. oneidensis*.  
148 In all, we identified OMEs and OMVs in 13 bacterial species (summarized in Table S1).

149

150 **I- The diverse forms of bacterial membrane structures**

151 Based on their features, we classified membrane projections into the following categories: **1)**  
152 tubular extensions with a uniform diameter and with an internal scaffold (Fig. 1 a & b); **2)** tubular  
153 extensions with a uniform diameter and without a clear internal scaffold (Fig. 1 c-g ); **3)** tubular  
154 extensions with a vesicular dilation at the tip (a teardrop-like structure) and irregular dark densities  
155 inside (Fig. 1h); **4)** tubular extensions with irregular diameter or pearling tubes (Fig. 2 a-g); **5)**  
156 interconnected chains of vesicles with uniform neck-like connectors (Fig. 2 h & i); **6)** budding or  
157 detached vesicles: budding vesicles were still attached to the membrane, while detached vesicles  
158 were observed near a cell and could have budded directly or from a tube that pearled (Fig. 3 a-d);  
159 **7)** nanopods: tubes of S-layer containing OMVs (Fig. 3 e-i). See Table S1 for a summary of these  
160 observations.

161

162 Scaffolded membrane tubes were observed only in *H. pylori* and had a uniform diameter of 40 nm.  
163 The *H. pylori* strain imaged (*fliP*<sup>\*</sup>) contains a naturally-occurring point mutation that disrupts the



164 function of FliP, the platform upon which other CORE proteins assemble [33–35]. In addition, the  
165 dataset contained other mutants in this *fliP*\* background including additional CORE proteins ( $\Delta$ *fliO*  
166 and  $\Delta$ *fliQ*), flagellar basal body proteins ( $\Delta$ *fliM* and  $\Delta$ *fliG*), and the tyrosine kinase required for  
167 expression of the class II flagellar genes ( $\Delta$ *flgS*) [36] (Figs. 1 a-b and 4). This suggests that the *H.*  
168 *pylori* membrane tubes are unrelated to the CORE-dependent nanotubes that mediate cytoplasmic  
169 exchange in *B. subtilis* and other species [18,24].

170  
171 Previously, *H. pylori* tubes were described as forming in the presence of eukaryotic host cells [15].  
172 Here, however, we observed tubes on *H. pylori* grown on agar plates in the absence of eukaryotic  
173 cells, suggesting that they also form in the absence of host cells. We observed some differences,  
174 though, from the tubes formed in the presence of host cells: the tube ends were closed, no clear  
175 lateral ports were seen, and the tubes were usually straight. While some of these tubes extended  
176 more than 0.5  $\mu$ m, we never observed pearling. However, in some tubes, the internal scaffold did  
177 not extend all the way to the tip, and its absence caused the tube to dilate (from 40 nm in the  
178 presence of the scaffold to 66 nm in its absence, see Fig. 4f). In some cases we also observed tubes  
179 stemming from vesicles resulting from cell lysis (Figs. 4f and S1).

180  
181 In *Flavobacterium anhuiense* and *Chitinophaga pinensis*, which are both endophytic species  
182 extracted from sugar beet roots, in addition to tubes with irregular diameter and OMVs, tubular  
183 extensions with a uniform diameter and a vesicular dilation (teardrop-like structure) were observed  
184 stemming from the sides of the cell (Fig. 1h). Interestingly, irregular dark densities were observed  
185 inside these teardrop-like extensions (Fig. 1h). Chains of vesicles connected by neck-like bridges  
186 were similarly observed in a single species: *Borrelia burgdorferi*. The bridges were consistently

187 ~14 nm in length and ~8 nm in width. Where chains were seen attached to the outer membrane, a  
188 neck-like connection was present at the budding site (Fig. 2h). Vesicles in each chain were of a  
189 uniform size, usually 35-40 nm wide (e.g. Fig. 2i), but occasionally larger (e.g. Fig. 2h).

190  
191 When both tubes and vesicles were observed in the same species, the tubes generally had a more  
192 uniform diameter than the vesicles, which were of variable sizes and often had larger diameters  
193 than the tubes (Figs. S2 & S3). In addition, when a tube pearled into vesicles, there was no clear  
194 correlation between the length of the tube and the initiation point of pearling, with some tubes  
195 extending for many micrometers without pearling while other, shorter tubes were in the process of  
196 forming vesicles (Movies S1, S2, S3 and Fig. 2e). While most pearling was seen at the tips of tubes,  
197 pearling occasionally occurred simultaneously at both proximal and distal ends of the same tube  
198 (Movie S3). With one exception, pearling was seen in all species with tubes of uniform diameter  
199 and no internal scaffold. The exception was lysed *Pseudoalteromonas luteoviolacea*, which had  
200 narrow tubes only 20 nm in diameter (Fig. 1g). Some lysed *P. luteoviolacea* contained wider,  
201 pearling tubes (Fig. 2c). Interestingly, the tubes of various *M. xanthus* strains (see Materials and  
202 Methods) and *P. luteoviolacea* could bifurcate into branches, each of which had a uniform diameter  
203 similar to that of the main branch (Movie S4 and Fig. 1d and Fig. S4).

204  
205 In *C. crescentus* tomograms, we identified structures very similar to the “nanopod” extensions  
206 previously reported in *D. acidovorans* [25]. These structures consist of a tube made of the S-layer  
207 encasing equally-spaced OMVs (Fig. 3 e-h and Movie S5). The diameter of the S-layer tubes was  
208 ~45 nm and vesicles exhibited diameters ranging from ~13-25 nm. The nanopods were seen either  
209 detached from the cell (Fig. 3 e-g), or budding from the pole of *C. crescentus* (Fig. 3h).

210 **II- Protein complexes associated with membrane structures.**

211 Next, we examined protein complexes associated with OMEs and OMVs that we could identify in  
212 our cryo-tomograms. These complexes fell into three categories: **1)** randomly-located complexes  
213 found on OMEs, OMVs and cells; **2)** randomly-located complexes observed only on OMEs and  
214 OMVs, and **3)** complexes exclusively located at the tip of OMEs/OMVs.

215

216 In the first category, we observed what appeared to be the OM-associated portion of the empty  
217 basal body of the type IVa pilus (T4aP) machinery in OMEs of *M. xanthus*. These complexes,  
218 which were also found in the OM of intact cells, did not exhibit a preferred localization within the  
219 tube (Fig. 5a & b).

220

221 The second category of protein complexes, observed only on MEs and not on cells, contained two  
222 structures. The first was a trapezoidal structure observed on purified OMVs of *S. oneidensis*. The  
223 structure was ~11 nm wide at its base at the membrane and was seen sometimes on the outside  
224 (Fig. 5c) and sometimes the inside of vesicles (Fig. 5 d). The second structure was a large crown-  
225 like complex. We first observed these complexes on the outer surface of membrane vesicles  
226 associated with lysed *M. xanthus* cells (Fig. 6a). Occasionally, they were also present on what  
227 appeared to be the inner leaflet of the inner membrane of lysed cells (Fig. 6b). The exact topology  
228 is difficult to determine, however, since the arrangement of inner and outer membranes can be  
229 confounded by cell lysis. The structure of this complex was consistent enough to produce a  
230 subtomogram average from nine examples, improving the signal-to-noise ratio and revealing  
231 greater detail (Fig. 6c). These crown-like complexes are ~40 nm tall with a concave top and a base  
232 ~35 nm wide at the membrane (Fig. 6c). No such complexes were seen on OMEs and OMVs

233 associated with intact *M. xanthus* cells. We identified a morphologically similar crown-like  
234 complex on the outside of some tubes and vesicles purified from *S. oneidensis* (Fig. 6d-f). However,  
235 this complex was smaller, ~15 nm tall and ~20 nm wide at its base. As these were purified  
236 OMEs/OMVs, we cannot know whether they stemmed from lysed or intact cells. Interestingly, we  
237 found a similar large crown-like structure associated with lysed cells of two other species in which  
238 we did not identify MEs, namely *Pseudomonas flexibilis* and *Pseudomonas aeruginosa* (Fig. 6g-j  
239 & S5).

240

241 In the third category, we observed a secretin-like complex in many tubes and vesicles of *F.*  
242 *johnsoniae*. In tubes attached to the cell, the complex was always located at the distal tip (Figs. 7  
243 & S6 and Movie S6). From 35 membrane tubes seen attached to cells, we identified a secretin-like  
244 complex at the tip of 25 of them (~70%). In OMEs disconnected from the cell, the secretin-like  
245 complex was always located at one end (Fig. 7b & e). In total, in 198 tomograms we identified 88  
246 secretin-like particles, none of which were located in the middle of a tube. As the MEs are less  
247 crowded than cellular periplasm and usually thinner than intact cells, we could clearly distinguish  
248 an extracellular density and three periplasmic densities in side views (red and purple arrows,  
249 respectively, in Fig. 7a). Top views showed a plug in the center of the upper part of the complex  
250 (yellow arrows in Fig. 7g & h). Subtomogram averaging revealed details of the complex, including  
251 the plug and a distinct lower periplasmic ring (Fig. 7i & j & S7). While the upper two periplasmic  
252 rings were clearly distinguishable in many of the individual particles (e.g. Fig. 7a), they did not  
253 resolve as individual densities in the subtomogram average (Fig. 7i). The extracellular density was  
254 not resolved at all in the average, suggesting flexibility in this part.

255

256 Previous studies showed that a species which belongs to the same phylum as *F. johnsoniae*, namely  
257 *Cytophaga hutchinsonii*, uses a putative T2SS to degrade cellulose [37]. Since *F. johnsoniae* also  
258 degrades polysaccharides and other polymers, we BLASTed the sequence of the well-  
259 characterized *V. cholerae* T2SS secretin protein, GspD (UniProt ID P45779), against the genome  
260 of *F. johnsoniae* and found a hit, GspD-like T2SS secretin protein (A5FMB4), with an e-value of  
261  $1e^{-9}$ . This result and the general morphological similarity of this secretin to the published structure  
262 of the T2SS [38] suggested that the complex we observed might be the secretin of a T2SS. We  
263 therefore compared our subtomogram average with the only available *in situ* structure of a T2SS,  
264 a recent subtomogram average of the *Legionella pneumophila* T2SS [38] (Fig. 7i-l). The two  
265 structures were generally similar in length and both had a plug in the upper part of the complex.  
266 However, we also observed differences between the two structures. In *L. pneumophila*, the widest  
267 part of the secretin (15 nm) is located near the plug close to the OM, and the lower end of the  
268 complex is narrower (12 nm). In *F. johnsoniae*, this topology is reversed, with the narrowest part  
269 near the plug and OM (Fig. 7i-l). Additionally, the lowest domain of the *L. pneumophila* secretin  
270 did not resolve into a distinct ring as we saw in *F. johnsoniae* and no extracellular density was  
271 observed in *L. pneumophila*, either in the subtomogram average or single particles [38].

272

273

274

275

276

277

278

279 **Discussion:**

280 Our results highlight the diversity of MEs and MVs structures that bacteria can form even within  
281 a single species (Fig. 8). For example, we saw two types of membrane tubes in lysed *P.*  
282 *luteoviolacea* cells: one narrower with a uniform diameter of 20 nm which did not pearl into  
283 vesicles, and one wider with a variable diameter that did pearl into vesicles (Fig. 1g and Fig. 2c),  
284 a distinction which suggests that these extensions play different roles. Similarly, interspecies  
285 differences likely reflect different functions. For instance, the tubes of *M. xanthus* were on average  
286 longer, more abundant and more branched than the MEs of other species (Movies S1 & S4), which  
287 is likely related to their role in communication between cells of this highly social species. However,  
288 one interesting observation in all the species we investigated here is that there was no clear  
289 distinctive molecular machine at the base of the membrane projections, raising the question of  
290 what drives their formation. This observation is consistent with a recent study which showed that  
291 liquid-like assemblies of proteins in membranes can lead to the formation of tubular extensions  
292 without the need for solid scaffolds [39].

293

294 The scaffolded uniform tubes of *H. pylori* that we observed were formed in samples not incubated  
295 with eukaryotic cells, indicating that they can also form in their absence. However, the tubes we  
296 found had closed ends and no clear lateral ports, while some of the previously-reported tubes  
297 (formed in the presence of eukaryotic host cells) had open ends and prominent ports [15]. It is  
298 possible that such features are formed only when *H. pylori* are in the vicinity of host cells. We also  
299 show that the tubes of *H. pylori* are CORE-independent, indicating that they are different from the  
300 CORE-dependent nanotubes described in other species.

301

302 A recent study showed that the formation of bacterial tubes significantly increases when cells are  
303 stressed or dying [28]. Consistent with this, in our cryo-tomograms we saw many MEs and MVs  
304 associated with lysed cells (such as in *H. pylori*, *H. hepaticus*, and *P. luteoviolacea*). We also saw  
305 tubes and vesicles stemming from intact cells. Given the nature of cryo-ET snapshots, we cannot  
306 tell whether a cell that appears intact is stressed, nor can we know whether MEs/MVs formed  
307 before or after a cell lysed. One observation which might be related to this issue comes from *F.*  
308 *johnsoniae* where tubes with regular diameters were seen stemming mainly from cells with a  
309 noticeably wavy OM (45 examples), while pearling tubes and OMVs stemmed primarily from  
310 cells with a smooth outer membrane (> 100 examples). Compare, for example, the cells in Figures  
311 1e and S6 and Movies S2 and S6 (wavy OM) to those in Figures 3d, 7a and f (smooth OM).

312  
313 In *C. crescentus*, we observed for the first time “nanopods,” a structure previously reported in *D.*  
314 *acidovorans* [25]. Both of these species are diderms with an S-layer, suggesting that nanopods  
315 may be a general form for OMVs in bacteria with this type of cell envelope. Nanopods were  
316 proposed to help disperse OMVs in the partially hydrated environment of the soil where *D.*  
317 *acidovorans* lives; it will be interesting to study their function in aquatic *C. crescentus*.

318  
319 Examining protein complexes associated with OMEs and OMVs, some seemed to reflect a  
320 continuation of the same complexes found on the membrane from which the extensions stemmed,  
321 such as the T4aP basal body in *M. xanthus* [40]. Others, however, were only observed on MEs and  
322 not on cells. This could be because the complexes are related to the formation of the MEs, or it  
323 might simply reflect the fact that these extensions are generally thinner and less crowded than the  
324 bacterial periplasm, making the complexes easier to see in cryo-tomograms. Interestingly, the

325 crown-like complex we observed in *M. xanthus*, *P. aeruginosa* and *P. flexibilis* was exclusively  
326 associated with the membranes of lysed cells; we never observed it on OMEs and OMVs stemming  
327 from intact cells in *M. xanthus*. We observed a morphologically-similar crown-like structure with  
328 different dimensions in purified naturally-shed MEs/MVs of *S. oneidensis*, where we cannot know  
329 whether they arose from intact or lysed cells. The crown-like structures are remarkably large and  
330 their function remains a mystery. Due to the disruption of membranes in lysed cells, the topology  
331 of these complexes is difficult to unravel. However, these structures share a morphological  
332 similarity to a membrane-associated dome protein complex recently described on the limiting  
333 membrane of the lamellar bodies inside alveolar cells [41].

334

335 Similarly, regarding the different, trapezoidal structure in *S. oneidensis*, the fact that it was seen  
336 on both the outside and inside of purified MVs suggests that some of the purified vesicles adopted  
337 an inside-out orientation during purification (a documented phenomenon [42]). Interestingly, the  
338 overall architecture and dimensions of this trapezoidal structure are reminiscent of those of a  
339 recently-solved structure of the *E. coli* polysaccharide co-polymerase WzzB [43]. We hope future  
340 investigation by methods like mass spectrometry will characterize these novel ME/MV-associated  
341 protein complexes.

342

343 In *F. johnsoniae*, we observed secretin-like particles at the tip of ~70% of tubes stemming from  
344 the OM. This strong spatial correlation suggests a role for the secretin-like complex in the  
345 formation of MEs in this species. Based on homology, the GspD-like T2SS secretin is a strong  
346 candidate for the complex. Interestingly, though, we did not identify any secretin-like (or full  
347 T2SS-like) particles in the main cell envelope of *F. johnsoniae* cells. While we could have missed



348 them in the denser periplasm compared to the less-crowded OMEs and OMVs, it is possible that  
349 the structures are specifically associated with the formation of OMEs in this species. As these MEs  
350 stem only from the OM, there is no IM- embedded energy source for the complex, suggesting that  
351 they are not functional secretion systems and raising the question of what function they may serve.  
352 It is possible that the OMVs and OMEs form to dispense of the secretin.

353  
354 These complexes also indicate that MEs/MVs may provide an ideal system to investigate  
355 membrane-embedded structures in their native environment at higher resolution. For example, it  
356 remains unclear how secretins of various secretion systems are situated within the outer membrane.  
357 All high-resolution structures were detergent solubilized, and most *in situ* structures have low  
358 resolution due to cell thickness [44]. Purifying *F. johnsoniae* OMVs and performing high-  
359 resolution subtomogram averaging on the secretin-like complex might shed light on this question.

360  
361 Early in the history of life, lipid vesicles and elementary protocells likely experienced destabilizing  
362 conditions such as repeated cycles of dehydration and rehydration [45]. The binding of prebiotic  
363 amino acids to lipid vesicles can help stabilize them in such conditions [46] and it is conceivable  
364 that with billions of years of evolution, variations of these stabilized lipid structures acquired roles  
365 that conferred fitness advantages on bacterial species in various environments. Today, the ability  
366 of bacteria to extend their membranes to form tubes or vesicles is a widespread phenomenon with  
367 many important biological functions. We hope that the structural classification we present here  
368 will serve as a helpful reference for future studies in this growing field.

369  
370

371 **References:**

- 372 1. Schwechheimer C, Kuehn MJ. Outer-membrane vesicles from Gram-negative bacteria:  
373 biogenesis and functions. *Nature Reviews Microbiology*. 2015;13: 605–619.  
374 doi:10.1038/nrmicro3525
- 375 2. Jan AT. Outer Membrane Vesicles (OMVs) of Gram-negative Bacteria: A Perspective  
376 Update. *Frontiers in Microbiology*. 2017;8. doi:10.3389/fmicb.2017.01053
- 377 3. D’Souza G, Shitut S, Preussger D, Yousif G, Waschina S, Kost C. Ecology and evolution of  
378 metabolic cross-feeding interactions in bacteria. *Natural Product Reports*. 2018;35: 455–  
379 488. doi:10.1039/C8NP00009C
- 380 4. Toyofuku M, Nomura N, Eberl L. Types and origins of bacterial membrane vesicles. *Nature*  
381 *Reviews Microbiology*. 2019;17: 13–24. doi:10.1038/s41579-018-0112-2
- 382 5. Pirbadian S, Barchinger SE, Leung KM, Byun HS, Jangir Y, Bouhenni RA, et al.  
383 *Shewanella oneidensis* MR-1 nanowires are outer membrane and periplasmic extensions of  
384 the extracellular electron transport components. *Proceedings of the National Academy of*  
385 *Sciences*. 2014;111: 12883–12888. doi:10.1073/pnas.1410551111
- 386 6. Subramanian P, Pirbadian S, El-Naggar MY, Jensen GJ. Ultrastructure of *Shewanella*  
387 *oneidensis* MR-1 nanowires revealed by electron cryotomography. *Proceedings of the*  
388 *National Academy of Sciences*. 2018;115: E3246–E3255. doi:10.1073/pnas.1718810115
- 389 7. Ducret A, Fleuchot B, Bergam P, Mignot T. Direct live imaging of cell–cell protein transfer  
390 by transient outer membrane fusion in *Myxococcus xanthus*. *eLife*. 2013;2.  
391 doi:10.7554/eLife.00868
- 392 8. Wei X, Vassallo CN, Pathak DT, Wall D. Myxobacteria Produce Outer Membrane-  
393 Enclosed Tubes in Unstructured Environments. *Journal of Bacteriology*. 2014;196: 1807–  
394 1814. doi:10.1128/JB.00850-13
- 395 9. Remis JP, Wei D, Gorur A, Zemla M, Haraga J, Allen S, et al. Bacterial social networks:  
396 structure and composition of *Myxococcus xanthus* outer membrane vesicle chains:  
397 Membrane vesicle chains and membrane network of *M. xanthus*. *Environmental*  
398 *Microbiology*. 2014;16: 598–610. doi:10.1111/1462-2920.12187
- 399 10. Reyes-Robles T, Dillard RS, Cairns LS, Silva-Valenzuela CA, Housman M, Ali A, et al.  
400 *Vibrio cholerae* Outer Membrane Vesicles Inhibit Bacteriophage Infection. DiRita VJ,  
401 editor. *Journal of Bacteriology*. 2018;200. doi:10.1128/JB.00792-17
- 402 11. Fischer T, Schorb M, Reintjes G, Kolovou A, Santarella-Mellwig R, Markert S, et al.  
403 Biopearling of Interconnected Outer Membrane Vesicle Chains by a Marine  
404 Flavobacterium. Cann I, editor. *Applied and Environmental Microbiology*. 2019;85.  
405 doi:10.1128/AEM.00829-19

- 406 12. Møller J, Barnes A, Dalsgaard I, Ellis A. Characterisation of surface blebbing and  
407 membrane vesicles produced by *Flavobacterium psychrophilum*. *Diseases of Aquatic*  
408 *Organisms*. 2005;64: 201–209. doi:10.3354/dao064201
- 409 13. McCaig WD, Koller A, Thanassi DG. Production of Outer Membrane Vesicles and Outer  
410 Membrane Tubes by *Francisella novicida*. *Journal of Bacteriology*. 2013;195: 1120–1132.  
411 doi:10.1128/JB.02007-12
- 412 14. Laanto E, Penttinen RK, Bamford JK, Sundberg L-R. Comparing the different morphotypes  
413 of a fish pathogen - implications for key virulence factors in *Flavobacterium columnare*.  
414 *BMC Microbiology*. 2014;14: 170. doi:10.1186/1471-2180-14-170
- 415 15. Chang Y-W, Shaffer CL, Rettberg LA, Ghosal D, Jensen GJ. In Vivo Structures of the  
416 *Helicobacter pylori* cag Type IV Secretion System. *Cell Reports*. 2018;23: 673–681.  
417 doi:10.1016/j.celrep.2018.03.085
- 418 16. Hampton CM, Guerrero-Ferreira RC, Storms RE, Taylor JV, Yi H, Gulig PA, et al. The  
419 Opportunistic Pathogen *Vibrio vulnificus* Produces Outer Membrane Vesicles in a Spatially  
420 Distinct Manner Related to Capsular Polysaccharide. *Frontiers in Microbiology*. 2017;8.  
421 doi:10.3389/fmicb.2017.02177
- 422 17. Brown L, Wolf JM, Prados-Rosales R, Casadevall A. Through the wall: extracellular  
423 vesicles in Gram-positive bacteria, mycobacteria and fungi. *Nature Reviews Microbiology*.  
424 2015;13: 620–630. doi:10.1038/nrmicro3480
- 425 18. Bhattacharya S, Baidya AK, Pal RR, Mamou G, Gatt YE, Margalit H, et al. A Ubiquitous  
426 Platform for Bacterial Nanotube Biogenesis. *Cell Reports*. 2019;27: 334-342.e10.  
427 doi:10.1016/j.celrep.2019.02.055
- 428 19. Dubey GP, Ben-Yehuda S. Intercellular Nanotubes Mediate Bacterial Communication.  
429 *Cell*. 2011;144: 590–600. doi:10.1016/j.cell.2011.01.015
- 430 20. Baidya AK, Bhattacharya S, Dubey GP, Mamou G, Ben-Yehuda S. Bacterial nanotubes: a  
431 conduit for intercellular molecular trade. *Current Opinion in Microbiology*. 2018;42: 1–6.  
432 doi:10.1016/j.mib.2017.08.006
- 433 21. Pande S, Shitut S, Freund L, Westermann M, Bertels F, Colesie C, et al. Metabolic cross-  
434 feeding via intercellular nanotubes among bacteria. *Nature Communications*. 2015;6.  
435 doi:10.1038/ncomms7238
- 436 22. Benomar S, Ranava D, Cárdenas ML, Trably E, Rafrafi Y, Ducret A, et al. Nutritional  
437 stress induces exchange of cell material and energetic coupling between bacterial species.  
438 *Nat Commun*. 2015;6: 6283. doi:10.1038/ncomms7283
- 439 23. Baidya AK, Rosenshine I, Ben-Yehuda S. Donor-delivered cell wall hydrolases facilitate  
440 nanotube penetration into recipient bacteria. *Nat Commun*. 2020;11: 1938.  
441 doi:10.1038/s41467-020-15605-1

- 442 24. Pal RR, Baidya AK, Mamou G, Bhattacharya S, Socol Y, Kobi S, et al. Pathogenic *E. coli*  
443 Extracts Nutrients from Infected Host Cells Utilizing Injectisome Components. *Cell*.  
444 2019;177: 683-696.e18. doi:10.1016/j.cell.2019.02.022
- 445 25. Shetty A, Chen S, Tocheva EI, Jensen GJ, Hickey WJ. Nanopods: A New Bacterial  
446 Structure and Mechanism for Deployment of Outer Membrane Vesicles. Hensel M, editor.  
447 PLoS ONE. 2011;6: e20725. doi:10.1371/journal.pone.0020725
- 448 26. Marguet E, Gaudin M, Gaudiard E, Fourquaux I, le Blond du Plouy S, Matsui I, et al.  
449 Membrane vesicles, nanopods and/or nanotubes produced by hyperthermophilic archaea of  
450 the genus *Thermococcus*. *Biochemical Society Transactions*. 2013;41: 436–442.  
451 doi:10.1042/BST20120293
- 452 27. Bar-Ziv R, Moses E. Instability and “Pearling” States Produced in Tubular Membranes by  
453 Competition of Curvature and Tension. *Physical Review Letters*. 1994;73: 1392–1395.  
454 doi:10.1103/PhysRevLett.73.1392
- 455 28. Pospíšil J, Vítovská D, Kofroňová O, Muchová K, Šanderová H, Hubálek M, et al.  
456 Bacterial nanotubes as a manifestation of cell death. *Nature Communications*. 2020;11.  
457 doi:10.1038/s41467-020-18800-2
- 458 29. Bos J, Cisneros LH, Mazel D. Real-time tracking of bacterial membrane vesicles reveals  
459 enhanced membrane traffic upon antibiotic exposure. *Science Advances*. 2021;7: eabd1033.  
460 doi:10.1126/sciadv.abd1033
- 461 30. Sivabalasarma S, Wetzel H, Nußbaum P, van der Does C, Beeby M, Albers S-V. Analysis  
462 of Cell–Cell Bridges in *Haloferax volcanii* Using Electron Cryo-Tomography Reveal a  
463 Continuous Cytoplasm and S-Layer. *Front Microbiol*. 2021;11: 612239.  
464 doi:10.3389/fmicb.2020.612239
- 465 31. Ding HJ, Oikonomou CM, Jensen GJ. The Caltech Tomography Database and Automatic  
466 Processing Pipeline. *Journal of Structural Biology*. 2015;192: 279–286.  
467 doi:10.1016/j.jsb.2015.06.016
- 468 32. Ortega DR, Oikonomou CM, Ding HJ, Rees-Lee P, Alexandria, Jensen GJ. ETDB-Caltech:  
469 A blockchain-based distributed public database for electron tomography. Promponas VJ,  
470 editor. PLoS ONE. 2019;14: e0215531. doi:10.1371/journal.pone.0215531
- 471 33. Fukumura T, Makino F, Dietsche T, Kinoshita M, Kato T, Wagner S, et al. Assembly and  
472 stoichiometry of the core structure of the bacterial flagellar type III export gate complex.  
473 Stock A, editor. PLoS Biology. 2017;15: e2002281. doi:10.1371/journal.pbio.2002281
- 474 34. Fabiani FD, Renault TT, Peters B, Dietsche T, Gálvez EJC, Guse A, et al. A flagellum-  
475 specific chaperone facilitates assembly of the core type III export apparatus of the bacterial  
476 flagellum. Stock A, editor. PLoS Biology. 2017;15: e2002267.  
477 doi:10.1371/journal.pbio.2002267

- 478 35. Minamino T, Kawamoto A, Kinoshita M, Namba K. Molecular Organization and Assembly  
479 of the Export Apparatus of Flagellar Type III Secretion Systems. Berlin, Heidelberg:  
480 Springer Berlin Heidelberg; 2019. doi:10.1007/82\_2019\_170
- 481 36. Lertsethtakarn P, Ottemann KM, Hendrixson DR. Motility and Chemotaxis in  
482 *Campylobacter* and *Helicobacter*. Annual Review of Microbiology. 2011;65: 389–410.  
483 doi:10.1146/annurev-micro-090110-102908
- 484 37. Wang X, Han Q, Chen G, Zhang W, Liu W. A Putative Type II Secretion System Is  
485 Involved in Cellulose Utilization in *Cytophaga hutchisonii*. Frontiers in Microbiology.  
486 2017;8. doi:10.3389/fmicb.2017.01482
- 487 38. Ghosal D, Kim KW, Zheng H, Kaplan M, Truchan HK, Lopez AE, et al. In vivo structure  
488 of the Legionella type II secretion system by electron cryotomography. Nature  
489 Microbiology. 2019 [cited 22 Nov 2019]. doi:10.1038/s41564-019-0603-6
- 490 39. Yuan F, Alimohamadi H, Bakka B, Trementozzi AN, Day KJ, Fawzi NL, et al. Membrane  
491 bending by protein phase separation. Proc Natl Acad Sci USA. 2021;118: e2017435118.  
492 doi:10.1073/pnas.2017435118
- 493 40. Chang Y-W, Rettberg LA, Treuner-Lange A, Iwasa J, Søgaard-Andersen L, Jensen GJ.  
494 Architecture of the type IVa pilus machine. Science. 2016;351: aad2001.  
495 doi:10.1126/science.aad2001
- 496 41. Klein S, Wimmer BH, Winter SL, Kolovou A, Laketa V, Chlanda P. Post-correlation on-  
497 lamella cryo-CLEM reveals the membrane architecture of lamellar bodies. Commun Biol.  
498 2021;4: 137. doi:10.1038/s42003-020-01567-z
- 499 42. Kaplan M, Narasimhan S, de Heus C, Mance D, van Doorn S, Houben K, et al. EGFR  
500 Dynamics Change during Activation in Native Membranes as Revealed by NMR. Cell.  
501 2016;167: 1241-1251.e11. doi:10.1016/j.cell.2016.10.038
- 502 43. Wiseman B, Nitharwal RG, Widmalm G, Högbom M. Structure of a full-length bacterial  
503 polysaccharide co-polymerase. Nat Commun. 2021;12: 369. doi:10.1038/s41467-020-  
504 20579-1
- 505 44. Weaver SJ, Ortega DR, Sazinsky MH, Dalia TN, Dalia AB, Jensen GJ. CryoEM structure  
506 of the type IVa pilus secretin required for natural competence in *Vibrio cholerae*. Nature  
507 Communications. 2020;11. doi:10.1038/s41467-020-18866-y
- 508 45. Damer B, Deamer D. Coupled Phases and Combinatorial Selection in Fluctuating  
509 Hydrothermal Pools: A Scenario to Guide Experimental Approaches to the Origin of  
510 Cellular Life. Life. 2015;5: 872–887. doi:10.3390/life5010872
- 511 46. Cornell CE, Black RA, Xue M, Litz HE, Ramsay A, Gordon M, et al. Prebiotic amino acids  
512 bind to and stabilize prebiotic fatty acid membranes. Proceedings of the National Academy  
513 of Sciences. 2019;116: 17239–17244. doi:10.1073/pnas.1900275116

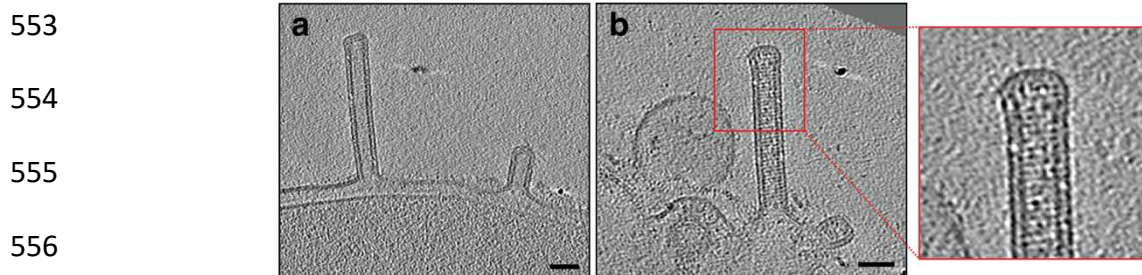
- 514 47. Kaplan M, Sweredoski MJ, Rodrigues JPGLM, Tocheva EI, Chang Y-W, Ortega DR, et al.  
515 Bacterial flagellar motor PL-ring disassembly subcomplexes are widespread and ancient.  
516 Proceedings of the National Academy of Sciences. 2020; 201916935.  
517 doi:10.1073/pnas.1916935117
- 518 48. Shikuma NJ, Pilhofer M, Weiss GL, Hadfield MG, Jensen GJ, Newman DK. Marine  
519 Tubeworm Metamorphosis Induced by Arrays of Bacterial Phage Tail-Like Structures.  
520 Science. 2014;343: 529–533. doi:10.1126/science.1246794
- 521 49. Cornejo E, Subramanian P, Li Z, Jensen GJ, Komeili A. Dynamic Remodeling of the  
522 Magnetosome Membrane Is Triggered by the Initiation of Biomineralization. mBio. 2016;7.  
523 doi:10.1128/mBio.01898-15
- 524 50. Phillips DA, Zacharoff LA, Hampton CM, Chong GW, Malanoski AP, Metskas LA, et al.  
525 A Prokaryotic Membrane Sculpting BAR Domain Protein. Microbiology; 2020 Jan.  
526 doi:10.1101/2020.01.30.926147
- 527 51. Briegel A, Ortega DR, Tocheva EI, Wuichet K, Li Z, Chen S, et al. Universal architecture  
528 of bacterial chemoreceptor arrays. Proceedings of the National Academy of Sciences.  
529 2009;106: 17181–17186. doi:10.1073/pnas.0905181106
- 530 52. Schrader JM, Shapiro L. Synchronization of *Caulobacter Crescentus* for Investigation of the  
531 Bacterial Cell Cycle. Journal of Visualized Experiments. 2015 [cited 15 Nov 2020].  
532 doi:10.3791/52633
- 533 53. Carrión VJ, Perez-Jaramillo J, Cordovez V, Tracanna V, de Hollander M, Ruiz-Buck D, et  
534 al. Pathogen-induced activation of disease-suppressive functions in the endophytic root  
535 microbiome. Science. 2019;366: 606–612. doi:10.1126/science.aaw9285
- 536 54. Zheng SQ, Keszthelyi B, Branlund E, Lyle JM, Braunfeld MB, Sedat JW, et al. UCSF  
537 tomography: an integrated software suite for real-time electron microscopic tomographic  
538 data collection, alignment, and reconstruction. J Struct Biol. 2007;157: 138–147.  
539 doi:10.1016/j.jsb.2006.06.005
- 540 55. Mastrorade DN. Automated electron microscope tomography using robust prediction of  
541 specimen movements. J Struct Biol. 2005;152: 36–51. doi:10.1016/j.jsb.2005.07.007
- 542 56. Rohou A, Grigorieff N. CTFFIND4: Fast and accurate defocus estimation from electron  
543 micrographs. Journal of Structural Biology. 2015;192: 216–221.  
544 doi:10.1016/j.jsb.2015.08.008
- 545 57. Kremer JR, Mastrorade DN, McIntosh JR. Computer visualization of three-dimensional  
546 image data using IMOD. J Struct Biol. 1996;116: 71–76. doi:10.1006/jsbi.1996.0013
- 547 58. Nicastro D. The Molecular Architecture of Axonemes Revealed by Cryoelectron  
548 Tomography. Science. 2006;313: 944–948. doi:10.1126/science.1128618

549

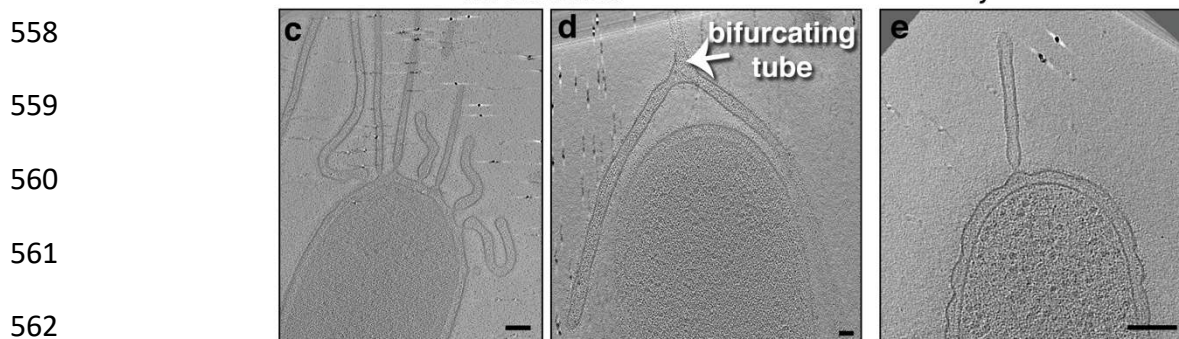


550 **Figures:**  
551 **Figure 1**

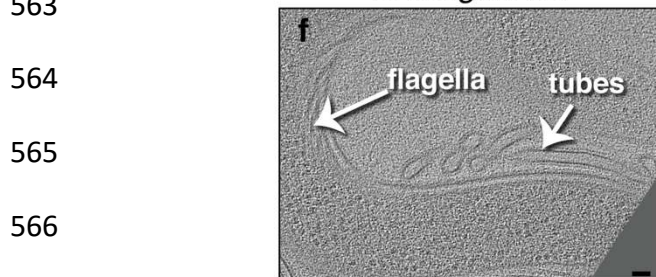
552 **Tubes with a uniform diameter and an internal scaffold**  
*H. pylori fljP\**



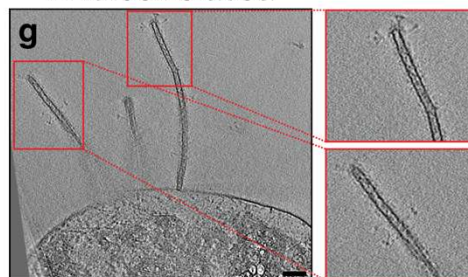
557 **Tubes with a uniform diameter and no clear internal scaffold**  
*M. xanthus* *F. johnsoniae*



563 *B. burgdorferi*

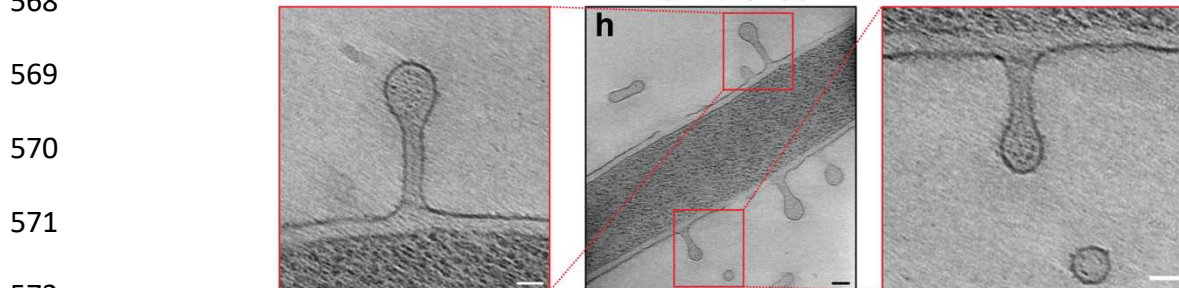


*P. luteoviolacea*



**Teardrop-like tubular extensions**

*F. anhuiense*



573

574 **Figure 2**

575

**Pearling tubes**

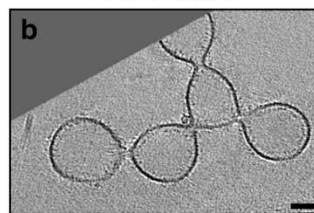
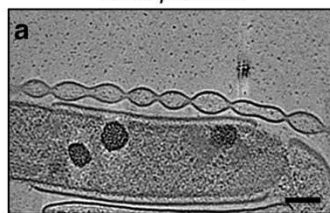
*H. hepaticus*

*S. oneidensis*

576

577

578



579

*P. luteoviolacea*

*H. gracilis*

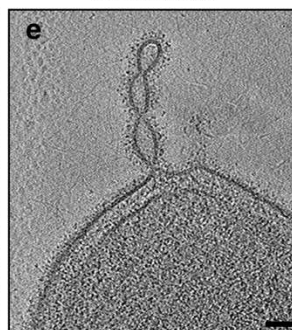
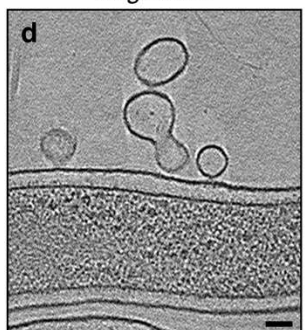
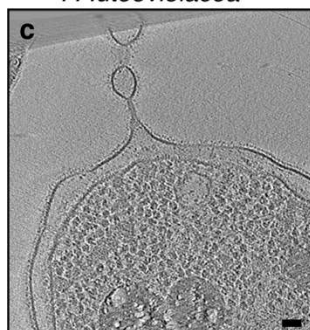
*M. xanthus*

580

581

582

583



584

**Tubes with irregular diameter**

*H. gracilis*

*C. pinensis*

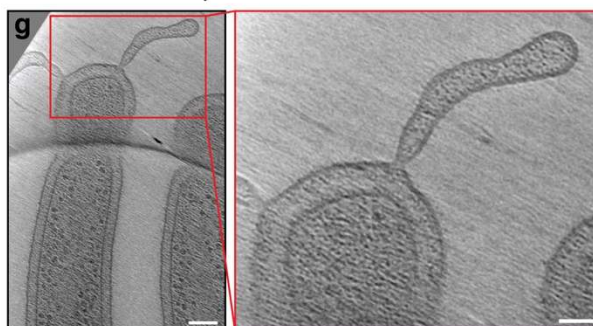
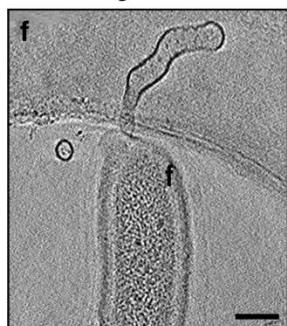
585

586

587

588

589



590

**Interconnected chains of vesicles with neck-like bridges**

*B. burgdorferi*

591

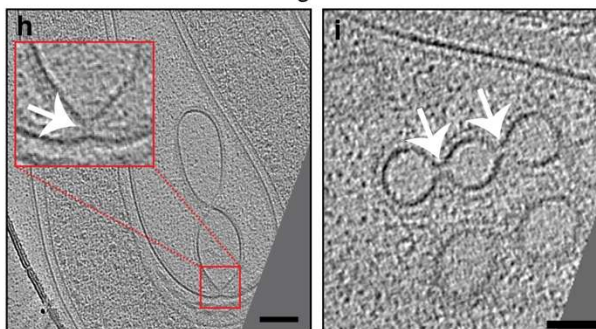
592

593

594

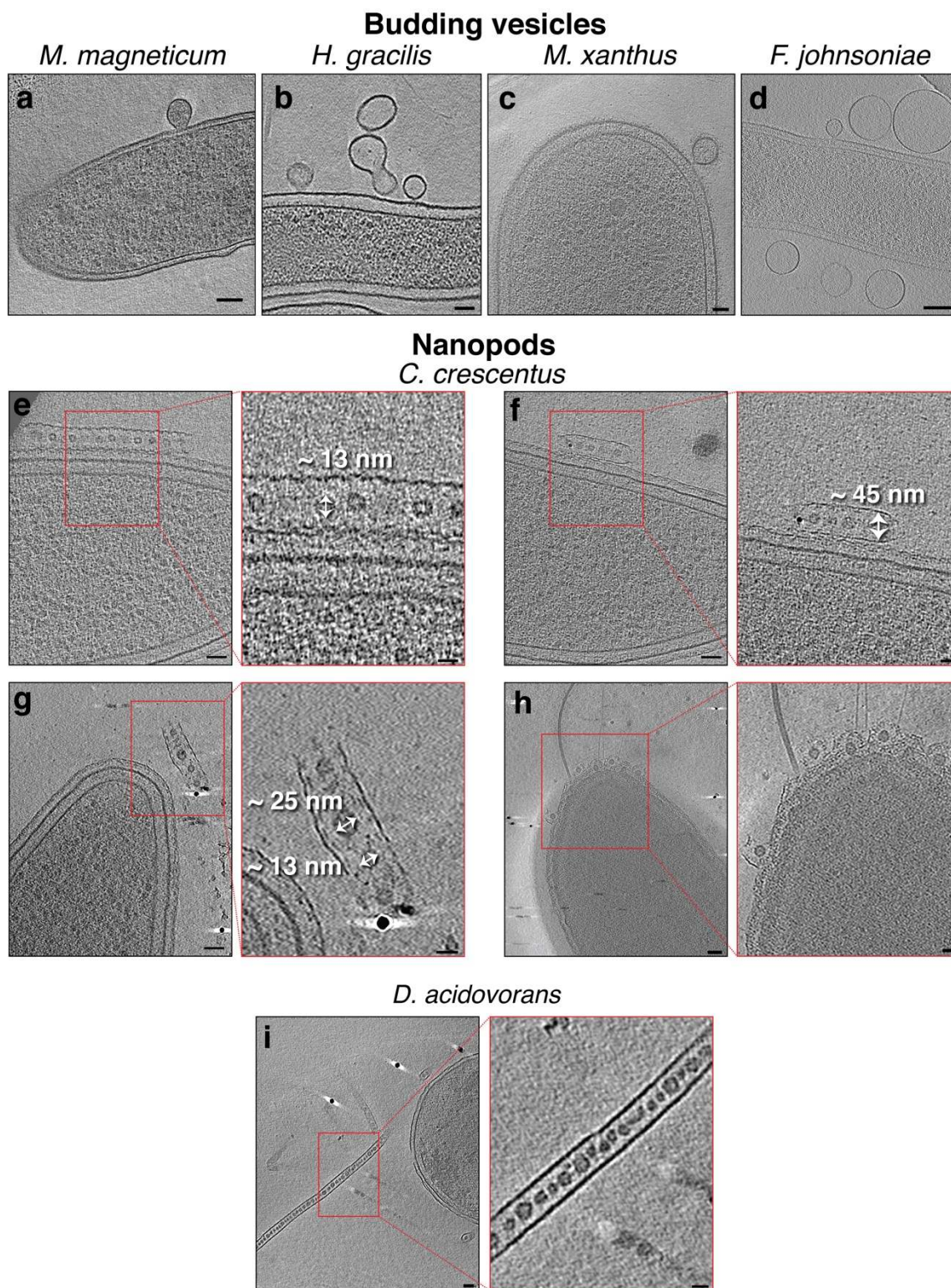
595

596





597 **Figure 3**



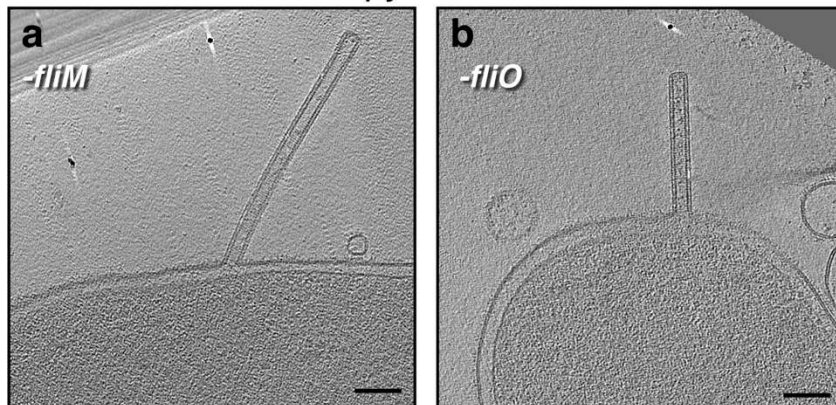


600 **Figure 4**

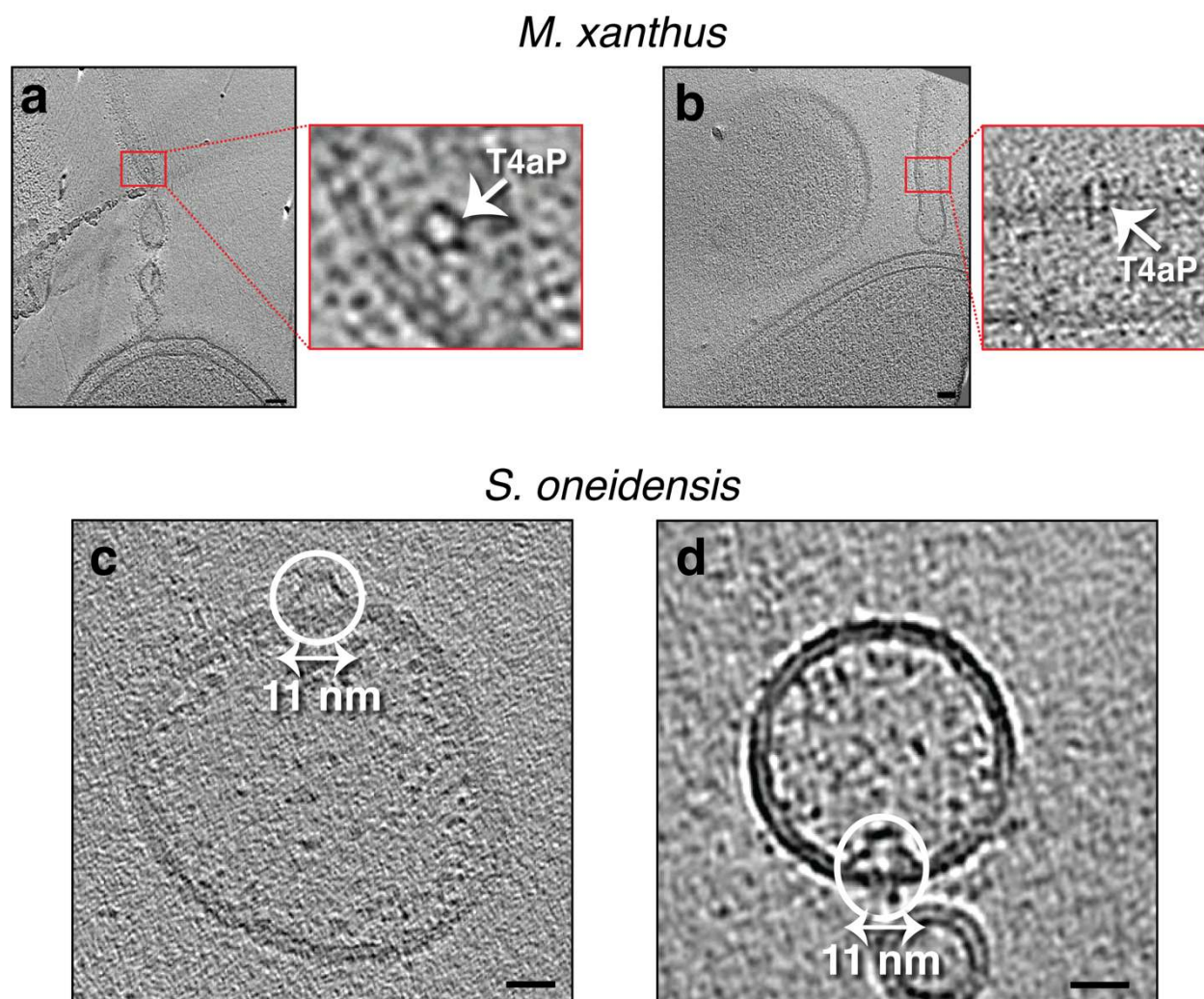
601

*H. pylori* *fliP*\*

602



623 **Figure 5**



624

625

626

627

628

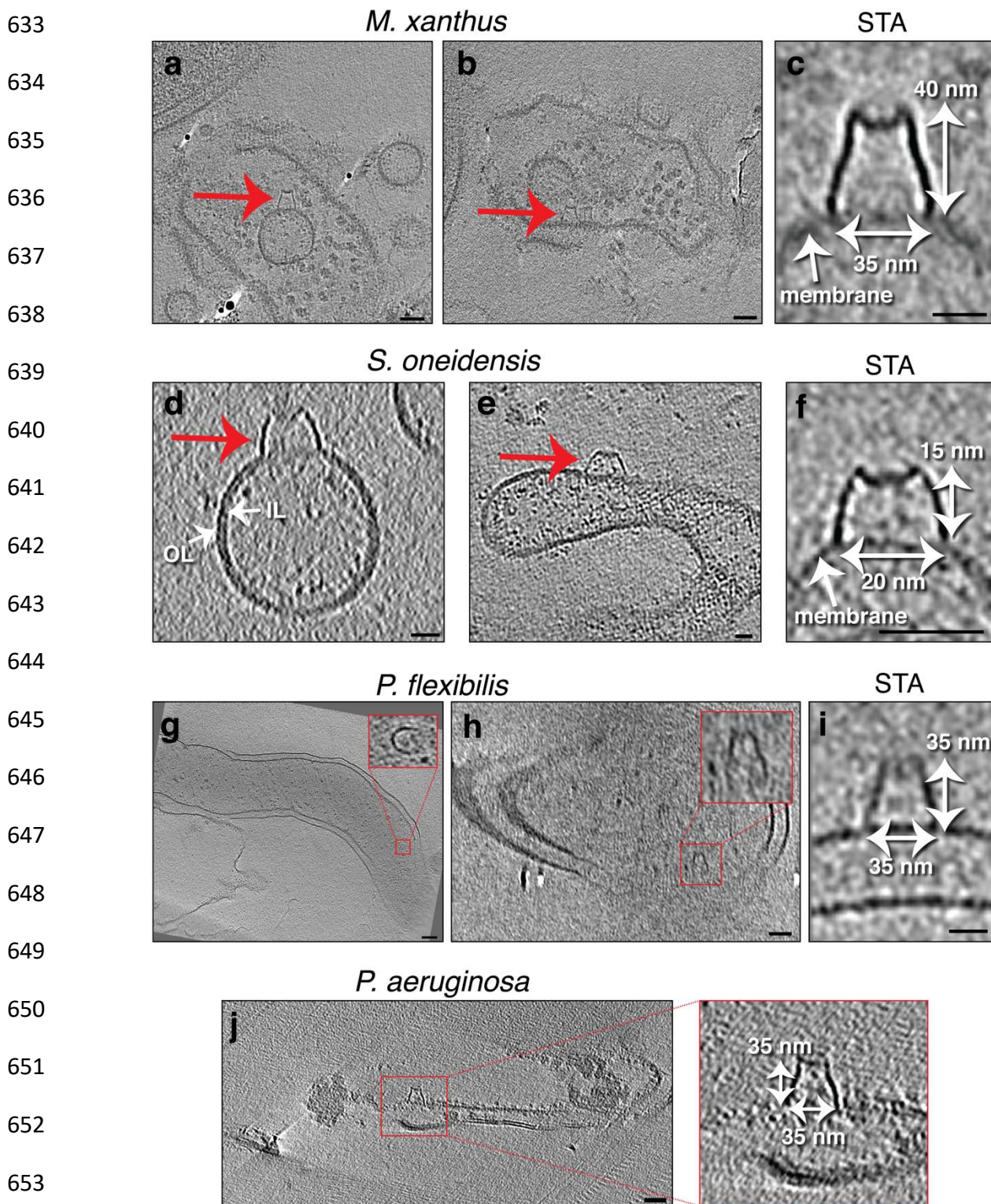
629

630

631



632 **Figure 6**

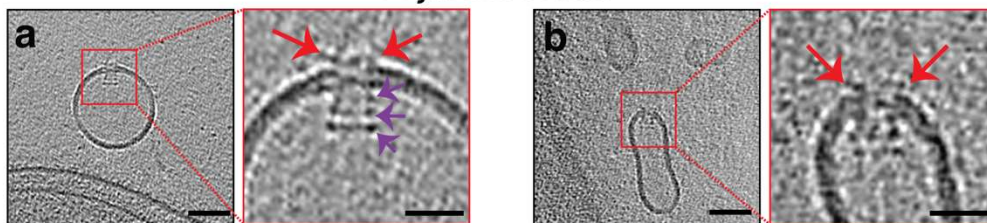


655 **Figure 7**

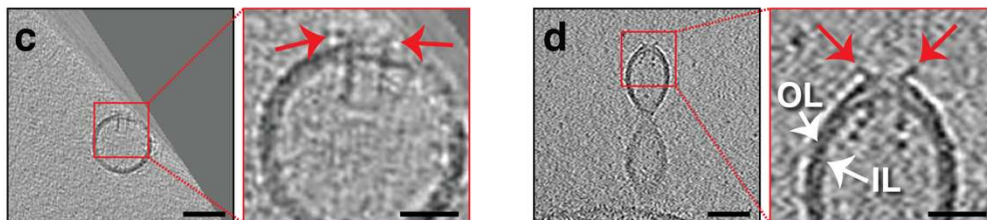
656

*F. johnsoniae*

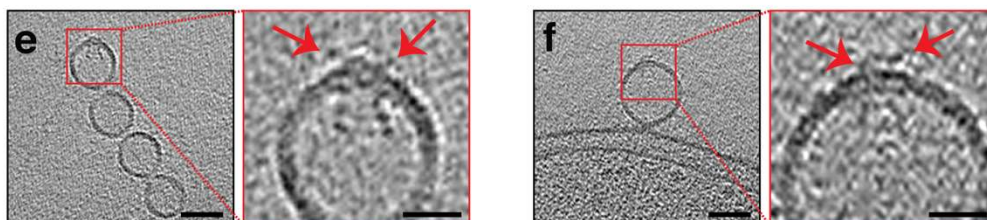
657



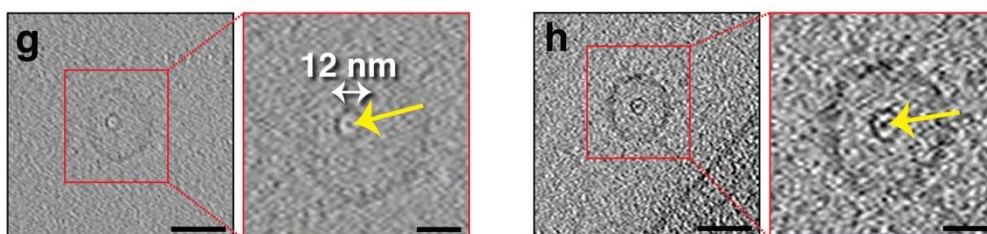
660



663



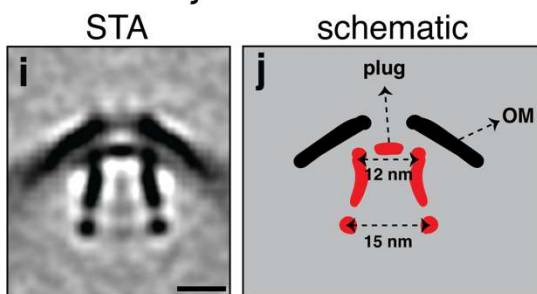
667



670

*F. johnsoniae*

671

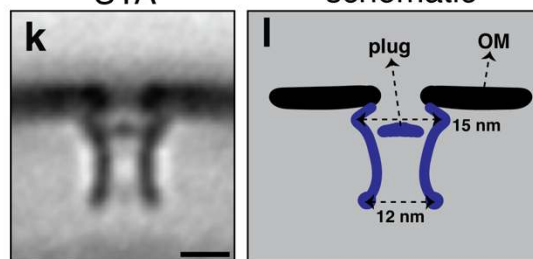


675

676

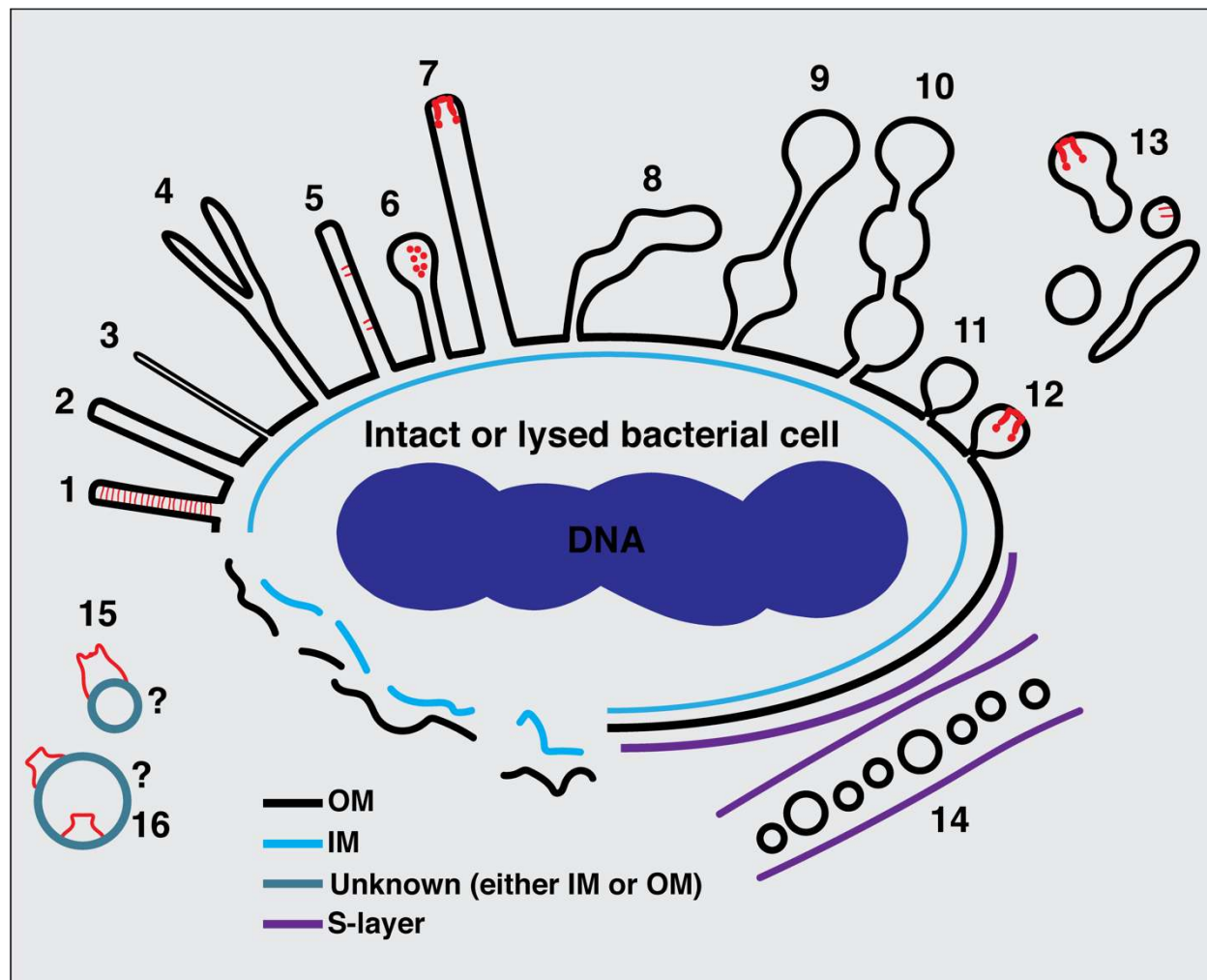
677

*L. pneumophila*





678 **Figure 8**



679

680

681

682

683

684

685

686

687

688 **Figure legends:**

689 **Figure 1: Membrane tubes with a uniform diameter, either with or without an internal**  
690 **scaffold.** Slices through electron cryo-tomograms of the indicated bacterial species highlighting  
691 the presence of OMEs with uniform diameters and either with **(a-b)** or without **(c-g)** an internal  
692 scaffold, and teardrop-like extensions **(h)**. In this and all subsequent figures, red boxes indicate  
693 enlarged views of the same slice. Scale bars are 50 nm, except in main panel **(h)** 100 nm.

694

695 **Figure 2: Pearling tubes, tubes with irregular diameter and vesicle chains with neck-like**  
696 **connections.** Slices through electron cryo-tomograms of the indicated bacterial species  
697 highlighting the presence of pearling tubes **(a-e)**, tubes with irregular diameter **(f-g)**, or OMV  
698 chains connected by neck-like bridges **(h-i)**. White arrows in the enlargement in **(h)** and in panel  
699 **(i)** point to the 14-nm connectors in *B. burgdorferi*. Scale bars are 50 nm, except in main panel **(g)**  
700 100 nm.

701

702 **Figure 3: Budding OMVs and nanopods.** Slices through electron cryo-tomograms of the  
703 indicated bacterial species highlighting the presence of budding vesicles **(a-d)** or nanopods **(e- i)**.  
704 Scale bars are 50 nm in main panels and 20 nm in enlargements.

705

706 **Figure 4: The formation of OM tubes persists in various *H. pylori* mutants, including CORE**  
707 **mutants.** Slices through electron cryo-tomograms of the indicated *H. pylori* mutants (all in the  
708 *fliP\** background) showing the presence of membrane tubes. The enlargement in **(f)** highlights a  
709 dilation at the end of the tube (dark blue arrow) due to the absence of the scaffold (orange arrow).  
710 Light blue arrows indicate the end points of the scaffold. Scale bars are 100 nm.

711 **Figure 5: Randomly-located protein complexes on OMEs of *M. xanthus* and purified MVs of**  
712 ***S. oneidensis*. a & b)** Slices through electron cryo-tomograms of *M. xanthus* indicating the  
713 presence of pearling tubes with top (a) and side (b) views of type IVa pilus basal bodies (T4aP).  
714 Scale bars are 50 nm. **c & d)** Slices through electron cryo-tomograms of purified *S. oneidensis*  
715 naturally-shed MEs and MVs highlighting the presence of trapezoidal structures on the outside (c)  
716 and inside (d) of vesicles. Scale bars are 10 nm.

717  
718 **Figure 6: Randomly-located protein complexes associated with lysed cells.** Slices through  
719 electron cryo-tomograms of lysed cells (**a, b, g, h & j**) or purified MEs and MVs (**d & e**) showing  
720 the presence of membrane vesicles and lysed membranes with a crown-like complex (red arrows  
721 and red-boxed enlargements). Scale bars: 50 nm (a, b, h and j), 100 nm (g), 10 nm (d and e). **c, f**  
722 **& i)** Central slices through subtomogram averages (with two-fold symmetry along the Y-axis  
723 applied) of 9 particles (c), 4 particles (f) or 3 particles (i) of the crown-like complex in the indicated  
724 species. Scale bars are 20 nm. OL=outer leaflet, IL=inner leaflet.

725  
726 **Figure 7: Secretin-like complexes located at the tip of OMEs and OMVs in *F. johnsoniae*.**  
727 Slices through electron cryo-tomograms of *F. johnsoniae* illustrating the presence of secretin-like  
728 complexes (side views in **a-f**, top views in **g & h** with yellow arrows pointing to the plug) in  
729 OMEs and OMVs of *F. johnsoniae*. Red arrows point to the extracellular part of the complex.  
730 Purple arrows in the enlargement in (a) point to the three periplasmic densities. Scale bars are 50  
731 nm in main panels and 20 nm in enlargements. **i)** A central slice through the subtomogram average  
732 of 88 particles of the secretin-like complex (with two-fold symmetry along the Y-axis applied).  
733 Scale bar is 10 nm. **j)** A schematic representation of the STA shown in (i). **k)** A central slice



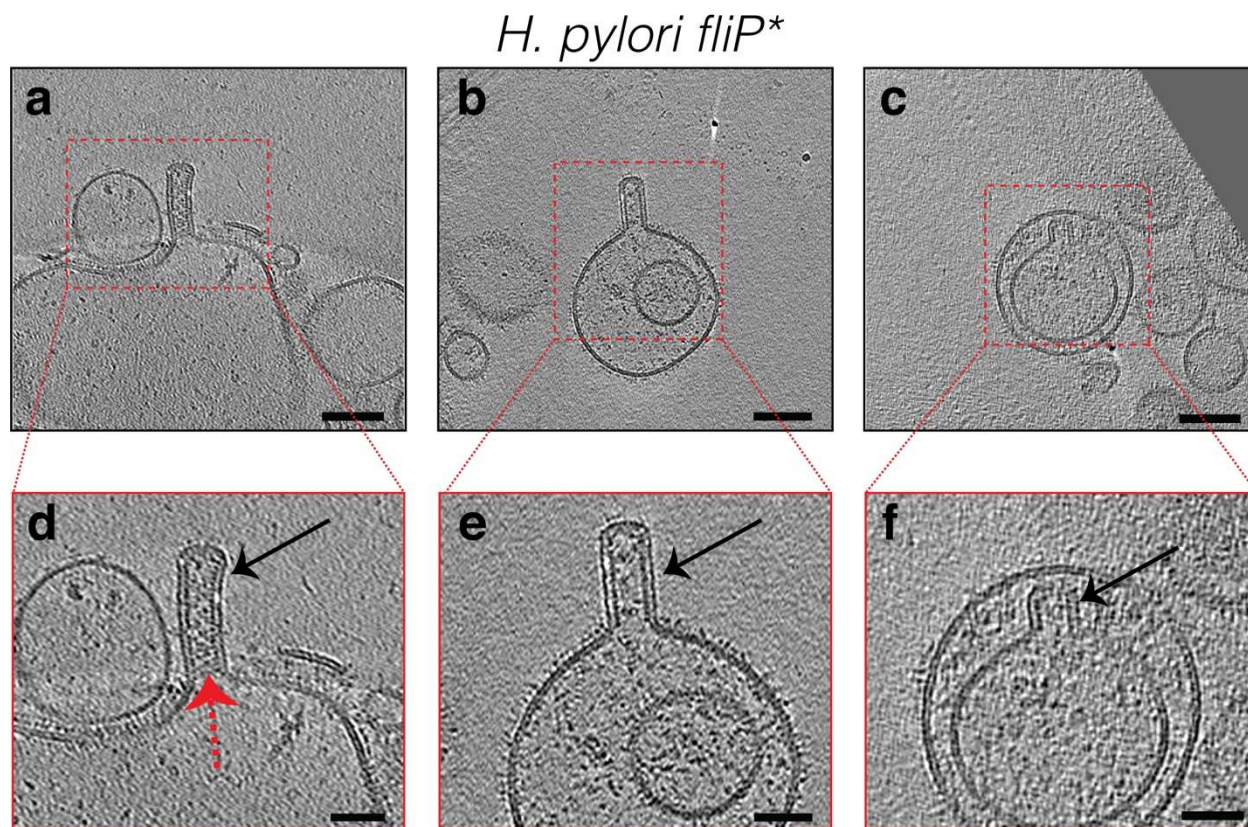
734 through the subtomogram average of the secretin of the T2SS of *L. pneumophila* (EMD 20713,  
735 see Ref. [38]). Scale bar is 10 nm. **l)** A schematic representation of the STA shown in (k).

736

737 **Figure 8: Summary of types of MEs and MVs identified in this study.** **1)** tubes with a uniform  
738 diameter and with an internal scaffold; **2 & 3)** tubes with a uniform diameter but without an internal  
739 scaffold; **4)** bifurcating tubes; **5)** tubes with randomly-located protein complexes (T4aP); **6)**  
740 teardrop-like extensions; **7)** tubes with a secretin-like complex at their tip; **8)** tubes with irregular  
741 diameter; **9)** pearling tubes; **10)** interconnected chains of vesicles with 14-nm connectors; **11)**  
742 budding vesicles; **12)** budding vesicles with a secretin-like complex at their tip; **13)** various  
743 disconnected membrane structures in the vicinity of bacterial cells; **14)** nanopods in species with  
744 an inner membrane (IM), outer membrane (OM), and S-layer; **15)** membrane structures with a  
745 crown-like complex from lysed cells; **16)** purified OMVs with trapezoidal complexes. The  
746 question marks in (15) and (16) indicate the difficulty of determining whether a membrane  
747 structure from lysed cells or purified vesicles originated from the IM or the OM or is in its original  
748 topology.

749

750 **Supporting information:**



751

752 **Figure S1:** Slices through electron cryo-tomograms of lysed *H. pylori* cells illustrating the  
753 presence of OM tubes in vesicles resulting from cell lysis (black arrows). Dashed red arrow in (d)  
754 points to the scaffold structure inside the tube. Scale bars are 100 nm in (a-c) and 50 nm in (d-f).

755

756

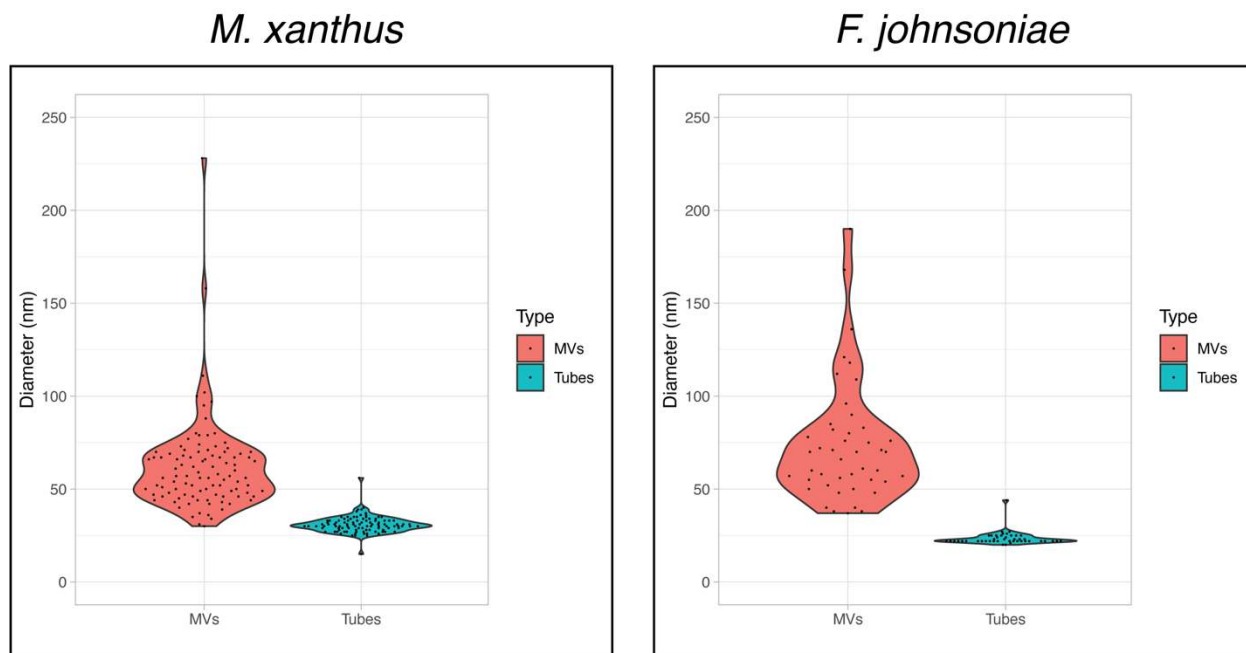
757

758

759

760

761



762

763 **Figure S2:** Violin plots of the sizes of OMVs and OM tubes in *M. xanthus* (100 randomly picked-  
764 examples of each) and *F. johnsoniae* (45 randomly-picked examples of each). For both species,  
765  $p < 0.001$  (determined using t-Test: Two-sample assuming unequal variances).

766

767

768

769

770

771

772

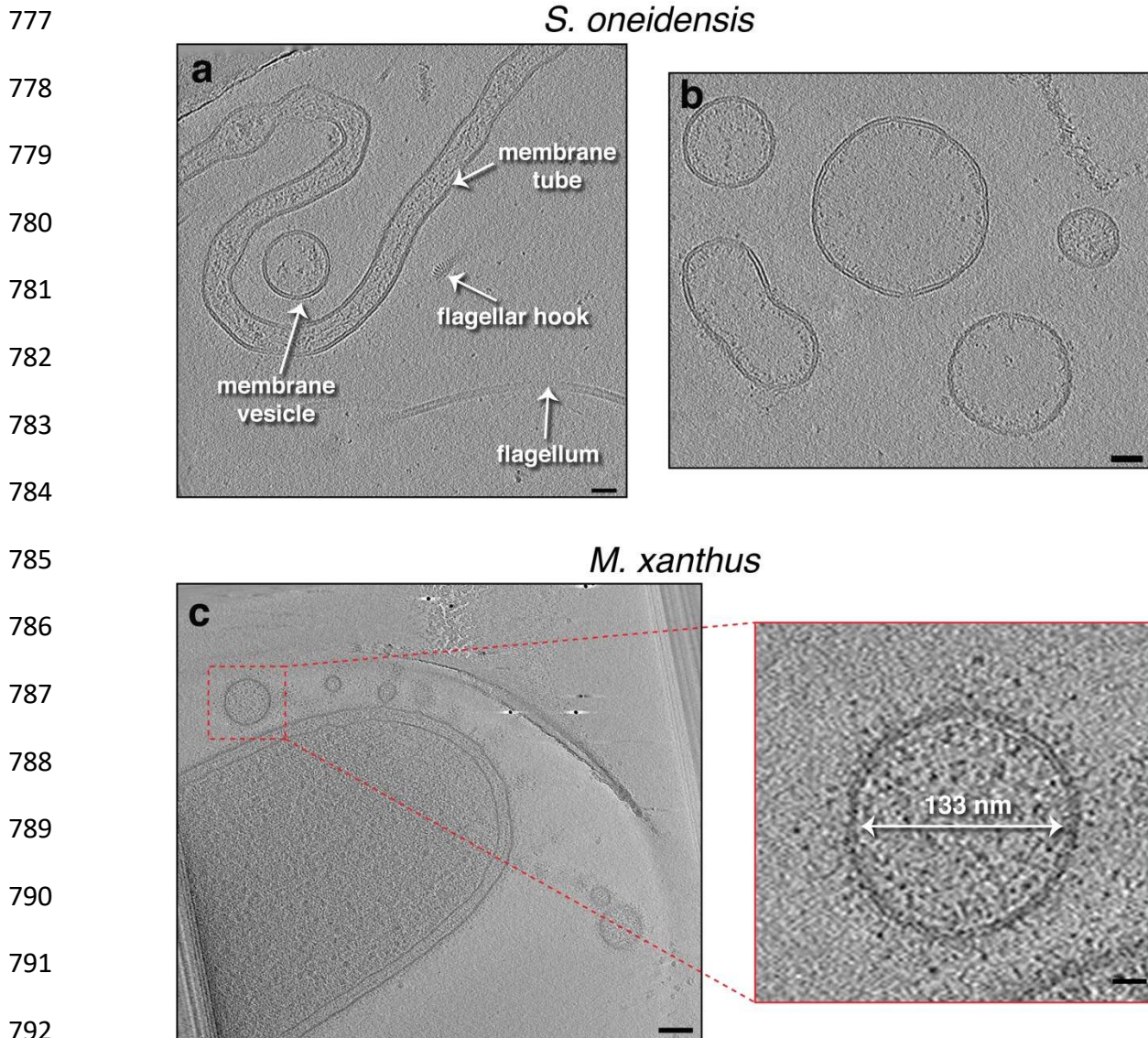
773

774

775

776





793 **Figure S3: a & b)** Slices through electron cryo-tomograms of purified MEs and MVs from *S.*  
794 *oneidensis*. Scale bars are 10 nm. **c)** A slice through an electron cryo-tomogram of an *M. xanthus*  
795 cell highlighting the presence of OMVs. Scale bar is 100 nm, and 20 nm in the enlargement on the  
796 right.

797

798

799

800  
801  
802  
803  
804  
805  
806  
807  
808  
809  
810  
811  
812  
813  
814  
815  
816  
817  
818  
819  
820  
821  
822



**Figure S4:** A slice through an electron cryo-tomogram of a lysed *P. luteoviolacea* cell illustrating a bifurcated 20-nm wide membrane tube. Scale bar is 50 nm. Dashed red line indicates a composite image of two slices through the tomogram at different z-heights.



823  
824  
825  
826  
827  
828  
829  
830  
831  
832  
833  
834  
835  
836  
837  
838  
839  
840  
841  
842  
843  
844  
845

*P. aeruginosa*

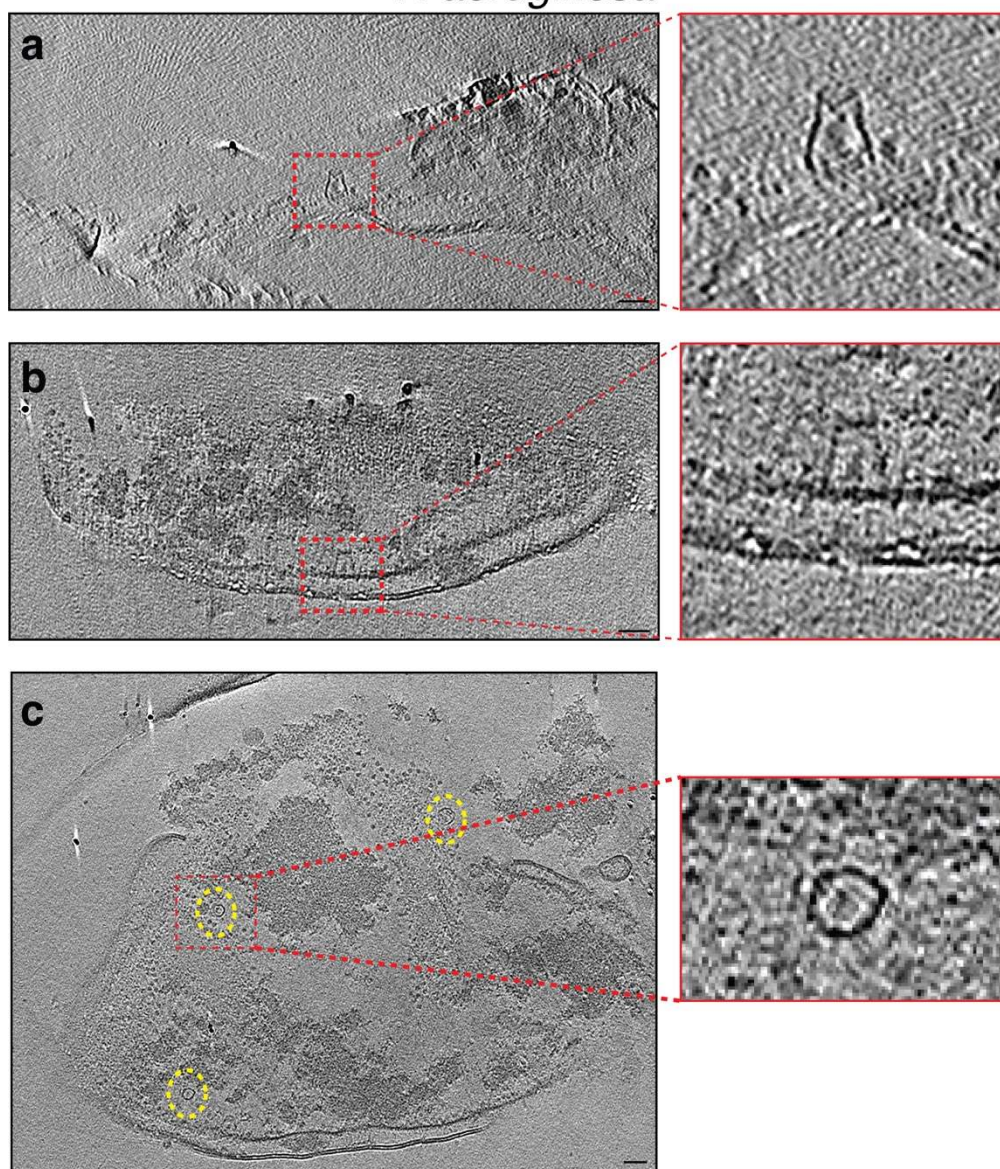
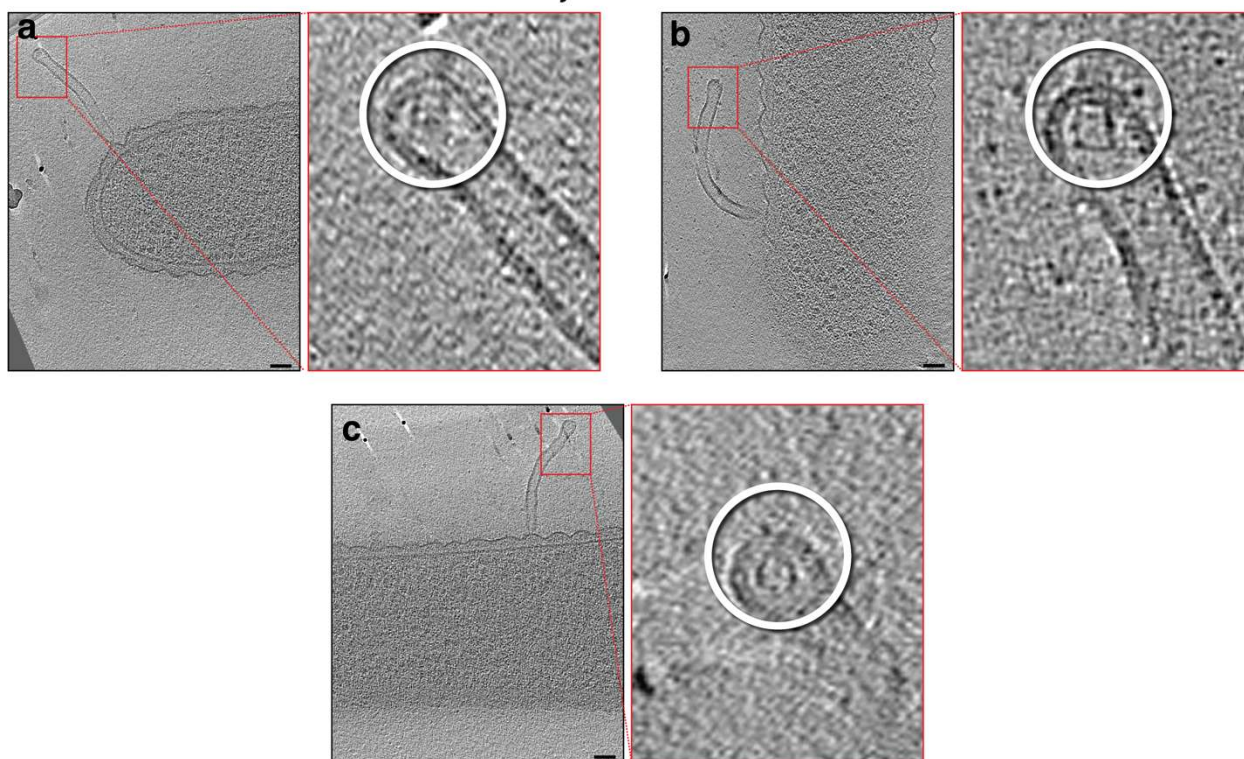


**Figure S5:** Slices through electron cryo-tomograms of lysed *P. aeruginosa* cells indicating the presence of crown-like structures in side views (**a & b**) and top view (**c**, dashed yellow ellipses). Panels on the right are enlargements of the boxed areas. Scale bars are 50 nm.

*F. johnsoniae*



846

847 **Figure S6:** Slices through electron cryo-tomograms of *F. johnsoniae* (with wavy OM) illustrating  
848 tubes stemming from cells with secretin-like complexes at their tips, as highlighted in the  
849 enlargements on the right (white circles). Note that the rotation of the slices on the left is optimized  
850 to show the full tube stemming from the cell, while the rotation of the enlargements on the right is  
851 optimized to show the best view of the secretin-like complex. Scale bars are 50 nm.

852

853

854

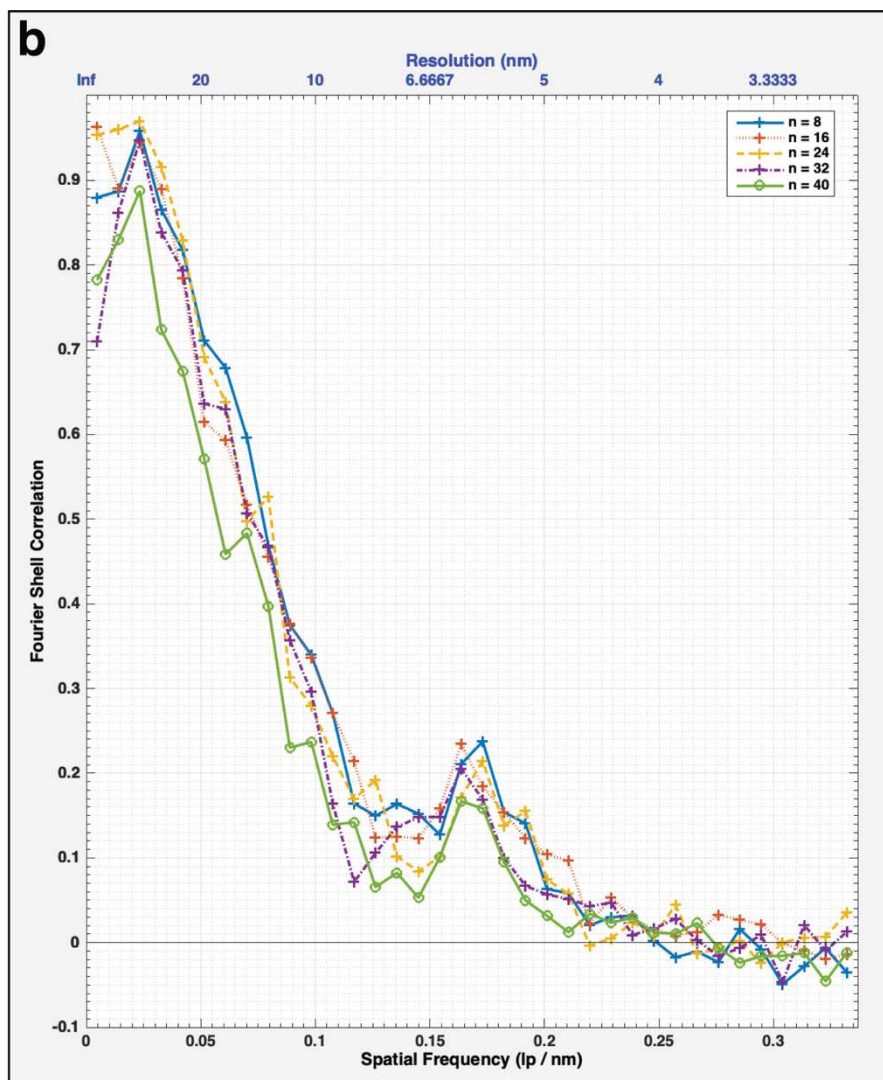
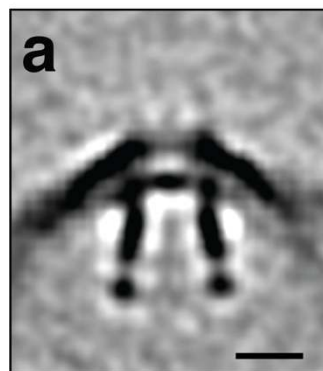
855

856

857

858





859

860 **Figure S7: a)** Central slice through the unsymmetrized subtomogram average of the secretin-like  
861 complex present in OM extensions in *F. johnsoniae*. Scale bar is 10 nm. **b)** FSC curve of the  
862 subtomogram average shown in (a). The different colored curves represent different subsets of  
863 particles.

864

865

866

867



868 **Supplementary movies:**

869

870 **Movie S1:** An electron cryo-tomogram of an *M. xanthus* cell with multiple outer membrane tubes  
871 stemming from the cell.

872

873 **Movie S2:** An electron cryo-tomogram of an *F. johnsoniae* cell with outer membrane tubes  
874 stemming from the cell. Note the wavy outer membrane of the cell.

875

876 **Movie S3:** An electron cryo-tomogram of an *M. xanthus* cell with a pearling outer membrane tube  
877 stemming from the cell.

878

879 **Movie S4:** An electron cryo-tomogram of an *M. xanthus* cell with multiple branched outer  
880 membrane tubes stemming from the cell.

881

882 **Movie S5:** An electron cryo-tomogram of a *C. crescentus* cell with a nanopod (black arrow) close  
883 to the cell.

884

885 **Movie S6:** An electron cryo-tomogram of an *F. johnsoniae* cell highlighting the presence of  
886 secretin-like particles at the tips of outer membrane tubes.

887

888

889

890

891 **Materials and Methods:**

892 **Strains and growth conditions**

893 *H. gracilis* cells were grown as described in reference [47]. *P. luteoviolacea* were grown as  
894 described in reference [48]. *M. magneticum* were grown as described in reference [49]. *P. flexibilis*  
895 706570 were grown in lactose growth medium. *Shewanella oneidensis* MR-1 cells were grown, as  
896 detailed in reference [50], in Luria Bertani (LB) media under aerobic conditions at 30°C with  
897 shaking at 200 rpm until they reached OD<sub>600</sub> of ~3. *Myxococcus xanthus* PiY1.3-sfGFP, *M.*  
898 *xanthus*  $\Delta$ *tsaP*, and *M. xanthus* SA6892 strains were grown as described in reference [40]. *Borrelia*  
899 *burgdorferi* B31 ATCC 35210 and *Helicobacter hepaticus* ATCC 51449 cells were grown in  
900 standard media (see reference [51] and references therein).

901

902 *Caulobacter crescentus* was cultured in M2G and M2 media (prepared as described in reference  
903 [52].) 5 mL of M2G were inoculated with a frozen stock of *C. crescentus* NA 1000 and grown  
904 overnight at 28 °C. 5 mL of the overnight culture was diluted in 15 mL M2G and grown at 28 °C  
905 with a shaking speed of 200 rpm for ~2 hours until mid-log phase (OD<sub>600</sub> 0.4-0.5). The sample  
906 was then centrifuged at 5200 x g for 6 minutes at 4 °C (same temperature for all subsequent  
907 centrifugation steps) and the pellet was resuspended in 1 mL M2 solution. The resuspended cells  
908 were transferred into a 2-mL microcentrifuge tube and centrifuged at 5200 x g for 5 minutes. All  
909 but ~250  $\mu$ L of supernatant was removed, 650  $\mu$ L M2 was added and the pellet was resuspended.  
910 900  $\mu$ L cold Percoll (Sigma Aldrich) was added and the sample was centrifuged at 15,000 x g for  
911 20 minutes. Samples were taken from the bottom of the tube to select swarmer cells.

912

913 Cells of *Flavobacterium johnsoniae* strain CJ2618 (a wild-type strain overexpressing FtsZ, ATCC  
914 17061) were taken from a glycerol stock, streaked onto a CYE plate with 10ug/mL tetracycline  
915 and grown at 25 °C. Subsequently, 5 mL of motility medium (MM) was inoculated with colonies  
916 from the plate and the culture was incubated at 25° C with 80 rpm shaking overnight. Then another  
917 5 mL MM was inoculated with 80 uL of starter culture and placed at 25° C with no shaking until  
918 the next day when the cells were harvested and prepared for plunge-freezing.

919  
920 *Helicobacter pylori* mutants ( $\Delta fliM fliP^*$ ,  $\Delta fliO fliP^*$ ,  $\Delta fliG fliP^*$ ,  $\Delta fliQ fliP^*$ ) were  
921 grown from glycerol stocks on sheep blood agar at 37 °C with 5% CO<sub>2</sub> for 48 hours and then either  
922 plunge-frozen directly or the cells were spread on another plate and left to grow for 24 hours before  
923 plunge-freezing. No difference could be discerned between the two samples by cryo-ET.

924  
925 *Flavobacterium anhuiense* (strain 98, see reference [53]) and *Chitinophaga pinensis* (strain 94,  
926 see reference [53]) cells were grown overnight in 1/10 TSB at 25°C and 300 rpm shaking in 50 ml  
927 cultures. For sample preparation, cells were first concentrated by centrifugation. 3 µL aliquots of  
928 the cell suspension were applied to glow-discharged R2/2 200 mesh copper Quantifoil grids  
929 (Quantifoil Micro Tools), the sample was pre-blotted for 30 seconds, and then blotted for 2.5  
930 seconds (*Flavobacterium anhuiense*) and 1 second (*Chitinophaga pinensis*). Grids were pre-  
931 blotted and blotted at 20 °C and at 95 % humidity. Subsequently, the grids were plunge-frozen in  
932 liquid ethane using an automated Leica EM GP system (Leica Microsystems) and stored in liquid  
933 nitrogen.

934

935

936 **Purification of *Shewanella oneidensis* OMVs**

937 *S. oneidensis* OMVs were purified as described in reference [50]. First, *S. oneidensis* were grown  
938 in LB media until they reached OD<sub>600</sub> of 3. Subsequently, the cells were centrifuged at 5000 x g  
939 for 20 minutes at 4°C; the pellet contained whole cells while the supernatant contained the OMVs.  
940 To remove any cells present in the supernatant, it was filtered through a 0.45 µm filter.  
941 Subsequently, the supernatant was centrifuged at 38,400 x g for one hour at 4°C; the OMVs were  
942 in the resultant pellet. The pellet was resuspended in 20 ml of 50 mM HEPES pH 6.8 buffer,  
943 filtered through a 0.22 µm filter, spun again as described above and ultimately resuspended in 50  
944 mM HEPES pH 6.8.

945

946 **Cryo-ET sample preparation and imaging**

947 For cellular samples, 10 nm gold beads were first coated with BSA (bovine serum albumin) and  
948 then mixed with the cells. Subsequently, 4 µl of this mixture was applied to a glow-discharged,  
949 thick carbon-coated, R2/2, 200 mesh copper Quantifoil grid (Quantifoil Micro Tools) in an FEI  
950 Vitrobot chamber with 100% humidity. Excess fluid was blotted away with filter paper and the  
951 grid was plunge-frozen in a mixture of ethane/propane. For the purified OMVs of *S. oneidensis*,  
952 the sample was first diluted to a 0.4 mg/ml concentration before it was applied to the grid [50].  
953 Cryo-ET imaging of the samples was done either on an FEI Polara 300-keV field emission gun  
954 transmission electron microscope equipped with a Gatan imaging filter and a K2 Summit direct  
955 electron detector in counting mode, or a Thermo Fisher Titan Krios 300-keV field emission gun  
956 transmission electron microscope equipped with a Gatan imaging filter and a K2 Summit counting  
957 electron detector. For data collection, either the UCSF Tomography [54] or SerialEM [55] software  
958 was used. For OMVs, tilt-series spanned -60° to 60° with an increment of 3°, an underfocus of 1-

959 5  $\mu\text{m}$ , and a cumulative electron dose of 121  $\text{e}/\text{\AA}^2$ . For *F. johnsoniae*, tilt-series spanned  $-55^\circ$  to  
960  $55^\circ$  with  $1^\circ$  increment, an underfocus of 4  $\mu\text{m}$ , a cumulative electron dose of 100  $\text{e}/\text{\AA}^2$ , and a 3.9  
961  $\text{\AA}$  pixel size. For *M. xanthus*, tilt-series spanned  $-60^\circ$  to  $60^\circ$  with an increment of  $1^\circ$ , an underfocus  
962 of 6  $\mu\text{m}$ , and a cumulative electron dose of 180  $\text{e}/\text{\AA}^2$ . For *B. burgdorferi*, tilt-series spanned  $-60^\circ$   
963 to  $60^\circ$  with  $1^\circ$  increment, an underfocus of 10  $\mu\text{m}$ , and a cumulative electron dose of 160  $\text{e}/\text{\AA}^2$ . For  
964 *H. hepaticus*, tilt-series spanned  $-60^\circ$  to  $60^\circ$  with increments of  $1^\circ$ , an underfocus of 12  $\mu\text{m}$ , and a  
965 cumulative electron dose of 165  $\text{e}/\text{\AA}^2$ .

966  
967 *Flavobacterium anhuiense* and *Chitinophaga pinensis* images were recorded with a Gatan K3  
968 Summit direct electron detector equipped with a Gatan GIF Quantum energy filter with a slit width  
969 of 20 eV. Images were taken at magnification corresponding to a pixel size of 3.28  $\text{\AA}$   
970 (*Chitinophaga pinensis*) and 4.4  $\text{\AA}$  (*Flavobacterium anhuiense*). Tilt series were collected using  
971 SerialEM with a bidirectional dose-symmetric tilt scheme ( $-60^\circ$  to  $60^\circ$ , starting from  $0^\circ$ ) with a  $2^\circ$   
972 increment. The defocus was set to  $-8-10 \mu\text{m}$  and the cumulative exposure per tilt series was 100  
973  $\text{e}/\text{\AA}^2$ . Images were reconstructed with the IMOD software package.

974

### 975 **Image processing and subtomogram averaging**

976 Reconstruction of tomograms of cellular samples was done using the automatic RAPTOR pipeline  
977 implemented in the Jensen laboratory at Caltech [31]. Tomograms of purified *S. oneidensis* OMVs  
978 were reconstructed using a combination of ctfind4 [56] and the IMOD software package [57].  
979 Subtomogram averaging was done using the PEET program [58], with 2-fold symmetry applied  
980 along the particle y-axis.

981



982 **Table S1:** A summary of the species included in this study and the major membrane structures  
 983 identified in each species.

Species	Class	Features Observed							
		Tubes				Vesicle chains		Budding/ vesicles	Nanopods
		<i>Uniform diameter - scaffold</i>	<i>Uniform diameter - no scaffold</i>	<i>Variable diameter</i>	<i>Pearling</i>	<i>Connectors</i>	<i>No connectors</i>		
<i>Shewanella oneidensis</i>	Gammaproteobacteria						see Ref [6]	>100	
<i>Pseudoalteromonas luteoviolacea</i>	Gammaproteobacteria		~100		~10				
<i>Hylemonella gracilis</i>	Betaproteobacteria			3	4			15	
<i>Delftia acidovorans</i>	Betaproteobacteria								see Ref [25]
<i>Magnetospirillum magneticum</i>	Alphaproteobacteria							49	
<i>Caulobacter crescentus</i>	Alphaproteobacteria								53
<i>Helicobacter hepaticus</i>	Epsilonproteobacteria				2				
<i>Helicobacter pylori</i>	Epsilonproteobacteria	>100							
<i>Myxococcus xanthus</i>	Deltaproteobacteria		>100		>100			>100	
<i>Borrelia burgdorferi</i>	Spirochaetes		9			19		16	
<i>Flavobacterium johnsoniae</i>	Flavobacteria		~45		~15			>100	
<i>Flavobacterium anhuiense</i>	Flavobacteria			5	7		4	>100 (including the teardrop-like extensions)	
<i>Chitinophaga pinensis</i>	Chitinophagia			11	12		3	81 (including the teardrop-like extensions)	

984

985 **Acknowledgements:**

986 This project was funded by the NIH (grant R35 GM122588 to G.J.J) and a Baxter postdoctoral  
987 fellowship from Caltech to M.K. Cryo-ET work was done in the Beckman Institute Resource  
988 Center for Transmission Electron Microscopy at the California Institute of Technology. We are  
989 grateful to Prof. Martin Pilhofer for collecting the *P. luteoviolacea* data and for critically reading  
990 the manuscript. We thank Prof. Elitza I Tocheva for collecting the *D. acidovorans* data. We thank  
991 Prof. Mohamed El-Naggar for insights into preparing *S. oneidensis* samples and Dr. Yuxi Liu for  
992 discussions. Briegel lab data was collected at the Netherlands Center for Electron Nanoscopy with  
993 support from Dr. Wen Yang. This data was collected with support from the National Roadmap for  
994 Large-Scale Research Infrastructure 2017 – 2018 with project number 184.034.014, which is  
995 financed in part by the Dutch Research Council (NWO). This work was also supported by the  
996 NWO OCENW.GROOT.2019.063 grant.

997

998